

## Chapter 4

# Laboratory Testing of SiPIN Detectors

Understanding and calibrating astronomical detectors in a laboratory environment before they are used to make measurements on the sky is essential. Not only does it help weed out broken parts or components that might be susceptible to damage when used continuously as part of an astronomical survey; characterizing a detector is crucial to understanding the signature it will impart on the data. For instance, the point spread function of the detector needs to be understood in order to make shape measurements of galaxies for the purpose of weak lensing studies.

In this chapter, standard characterization tests for an imaging detector are described in theory and measurements for HyViSI devices are presented. These standard tests include pixel operability, conversion gain and nodal capacitance, read noise, dark current, quantum efficiency, linearity, and well depth. Although pixel crosstalk and persistence are typically included in this list, these subjects are saved for later chapters as they entail a great deal of complexity. Before delving into these matters, we begin by describing the test systems that were used to carry out these tests.

### 4.1 Description of Laboratory Setups and Devices Tested

Most of the laboratory work done for this thesis was performed at the Rochester Imaging Detector Laboratory (RIDL) at the Rochester Institute of Technology (RIT). The RIDL system (see Figure 4.1) consists of software and hardware similar to that described in Figer et al. [62]. The modular architecture of the system allows for rapid acquisition and reduction of large datasets over a broad range of experimental conditions. Minimal effort is required to change between different detectors and different types of detectors, and the system can be transported for operation on a telescope.

The RIDL system includes a 16 inch diameter dewar (Universal Cryogenics, Tucson, AZ) with a

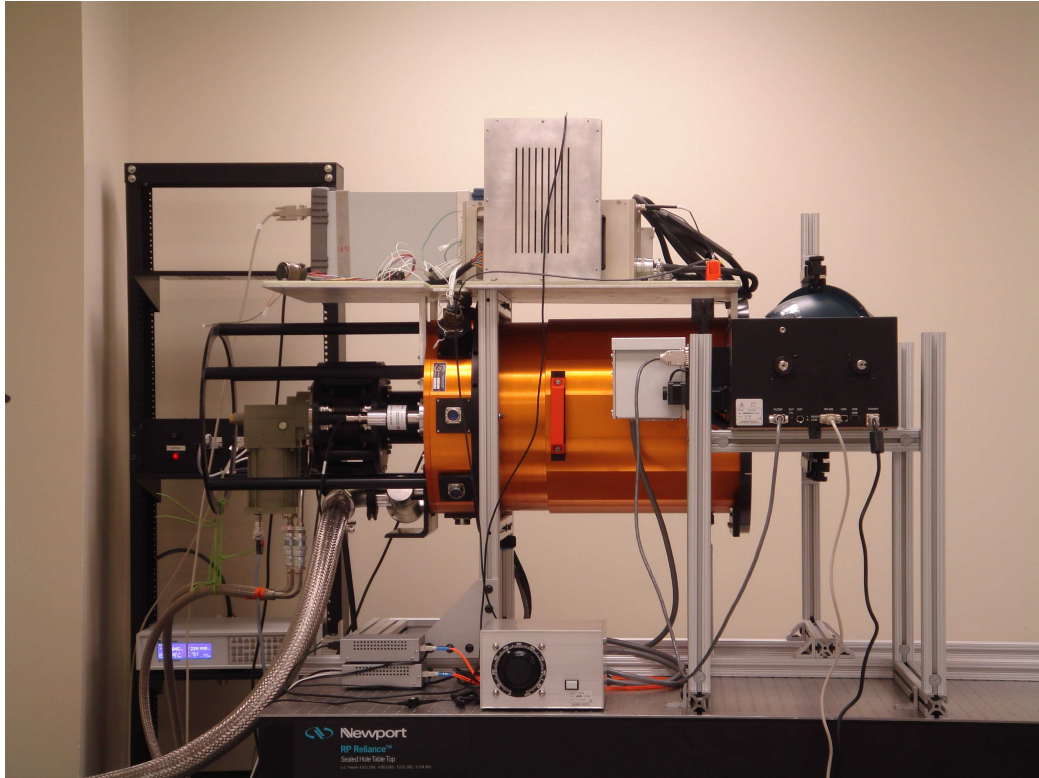


Figure 4.1: RIDL system. An orange dewar houses two filter wheels and a detector enclosure. A helium cryo-cooler cools the system. The picture shows an integrating sphere and monochromator near the front of the dewar. Post-processing electronics are mounted on a plate attached to the top side of the dewar. Off camera are three computers (two four-way and one eight-way CPU) with 4 GB, 12 GB, and 16 GB of RAM and 12 TB of RAID5 storage.

110 mm diameter CaF<sub>2</sub> window, two cryogenic filter wheels, and a detector enclosure. The system is cooled with a two-stage cooler (CTI Model 1050, Brooks Automation, Chelmsford, MA), and the detector is thermally stabilized with a 10-channel temperature controller (Lakeshore Cryotronics, Westerville, OH). The detector enclosure provides thermal and electrical feedthroughs and a light-tight cavity for the detector. The filter wheels can accommodate eight filters and/or radiation sources. We used two sets of readout electronics with this setup: 1) the Generation III electronics from Astronomical Research Cameras, Inc. (San Diego, CA), and 2) the room temperature SIDECAR ASIC from Teledyne Scientific & Imaging, LLC (Thousand Oaks, CA). A variety of programmable gains were used on each set of electronics. Unless otherwise noted, the data were recorded using a 5  $\mu$ s pixel time for the ARC electronics and 10  $\mu$ s pixel time for the SIDECAR. These correspond to 200 kHz and 100 kHz, respectively.

Additional measurements were performed at Teledyne Imaging Sensors (TIS) with a small custom dewar. The only electronic components inside the dewar, aside from standard silicon diode temperature sensors, were an H2RG detector and a cryogenic SIDECAR ASIC. Although the cryogenic SIDECAR, powered by a linear power supply instead of USB power, provided better noise performance than the room temperature SIDECAR kit used at RIDL, this setup was far more prohibitive in terms of the available tests that could be performed. There was no entry window into the dewar, so no light could be shined from outside. An attempt to place an LED inside of the dewar failed because its power supply created approximately 200 microvolts of noise, and limited testing time precluded the option of placing a light source inside to project a well sized spot of light for persistence measurements. However, an  $\text{Fe}^{55}$  source was made available for x-ray characterization, and very low noise dark current and single pixel reset measurements were performed.

The last setup from which measurements were obtained was a temporary one in the LSST laboratory at Stanford University. This system was composed of one of the LSST test dewars (also from Universal Cryogenics) on loan from Purdue University and an H2RG detector borrowed from Teledyne. Its primary purpose was to serve as a testbed for the LSST guider system, with a laser projection system delivering a small FWHM beam through a 6.5" pure fused silica window to the detector in order to simulate a guide star. Only a small fraction of the data from this detector and setup will be discussed—primarily to highlight a reduction in the Interpixel Charge Transfer (IPCT) discussed in Section 6.1.2—since ample time was not available to do rigorous analysis.

A list of the detectors that were tested in these various settings is shown in Table 4.1. The table includes the time period over which they were tested and where the testing was done. With the exception of H2RG-001 and H1RG-022, the dates correspond roughly to the newest technology available at the time, and thus, improvements in the HyViSI processing. For instance, a new type of surface treatment was used with H2RG-148 that significantly reduced the charge loss from IPCT seen in the previous devices. Other metrics were fairly consistent over all the detectors (aside from the H4RG), and all showed the same characteristics in image persistence.

HyViSI Detector	Pixel Size ( $\mu\text{m}$ )	Locations Tested	Dates of Testing
H1RG-022	18	RIDL, KPNO	3/07-7/08
H2RG-32-147	18	RIDL, KPNO	11/07-4/08
H2RG-001	18	TIS	11/08-12/08
H2RG-148	18	Stanford	7/09-8/09
H4RG-10-007	10	RIDL, KPNO	3/07-9/07

Table 4.1: A list of the various detectors studied in the laboratory for this thesis work. KPNO indicates that the device was also tested at the Kitt Peak 2.1m telescope.

## 4.2 Pixel Classification and Operability

The percentage of good pixels on a detector is called *pixel operability* [63]. It is a key figure of merit for both ground and space based astronomy missions. When a focal plane array is constructed, it is desirable to start out with the lowest fraction of bad pixels possible since some of the good ones will inevitably fail after prolonged use or bombardment with radiation, especially in the environment of space [64, 12]. Operability is usually specified as a detector requirement in the initial planning stages of a mission. For instance, the James Webb Space Telescope requires 98% operability for its science arrays [65].

There are several distinct types of pixels on the HyViSI detectors that are not suitable for scientific measurements. These pixels cannot be used to estimate the signal from a source without applying some correction, and in some instances, they cannot be used at all. They are categorized as dead, hot, and open pixels. In analyzing science data, these pixels are masked and not used. All of the other pixels on the detector are of suitable quality to be used in the science data analysis.

### 4.2.1 Dead or Railed Pixels

The first type of unusable pixels are “dead” pixels that do not increase in signal, no matter how much light they see. Most of them are railed at the high end of the detector voltage range, suggesting they are shorted to one of the high bias voltages. A substantial fraction of them also fall at the center of very high dark current clusters, sometimes referred to as “volcanoes”. These pixels are easy to detect since they do not show an increase in signal over time. In order to find them, we take differences between a read  $r$  and the first read  $r = 1$  from median flat field images and flag pixels that had a difference in signal,  $I_{Diff}(x, y)$ , below a certain threshold  $T$ . I.e.

$$I_{Diff}(x, y) = I(x, y, r) - I(x, y, 0) < T, \quad (4.1)$$

for all  $r$ .  $T$  depends on the gain of the pre-amps in the SIDECAR ASIC, but is typically set at  $3\sigma_r$ , where  $\sigma_r$  is the read noise of the detector at that gain.

For H2RG-32-147, nearly all of the dead pixels are found in volcanoes. For H4RG-10-007, the number includes an entire row of 4096 pixels that is presumably a bad line in the ROIC.

### 4.2.2 Hot Pixels

The hot pixels are found by (1) looking for very high pixel signal slopes,  $\Delta I/\Delta t$ , in UTR exposures and (2) looking for pixels that have a value of  $I$  greater than 75% of the full A/D range in the first read of median dark exposures. In the latter case, the dark current is so extreme that the pixel voltage reaches the upper rail almost immediately after reset, and its slope is flattened before the first read. For (1), pixels are flagged if they have a dark current greater than  $10 \text{ e}^-/\text{s}/\text{pix}$ .

### 4.2.3 Open Pixels

Open pixels are pixels that have a value that falls significantly below that of their nearest neighbors in well-illuminated images. I.e.

$$I(x, y, r) \ll I(x \pm 1, y \pm 1, r). \quad (4.2)$$

These pixels are presumed to be open in the sense that the indium bump bond does not connect the silicon substrate to the ROIC. Their spatial distribution over the detector is not uniform, and it has been mapped to a set of suspected opens by the manufacturer: Teledyne Scientific and Imaging. The fraction of open pixels on each of the HyViSI detectors tested are listed in Table 4.2.

Figure 4.2 illustrates how the open pixels appear in a typical image. The image, generated by subtracting the first read from the last read of a flat field exposure, shows isolated black squares and black squares surrounded by neighbors with enhanced signal. We associate the former with hot pixels since we have verified that their signal quickly reaches saturation such that they appear dark in a difference image. The open pixels are the black ones with bright neighbors. They see a very reduced rate of signal increase relative to *both* the background pixels and neighbors.

While the open pixels appear to be dead in the stretch shown in the figure, they do have increasing signal versus read number, but the slope may be anywhere in the range of 5-70% of the mean slope for regularly behaving pixels. Also, their neighbors have an elevated signal with respect to the regularly behaving pixels. This effect cannot be due to conventional interpixel capacitance because the open pixels have both a consistently low *raw voltage* relative to the neighbors *and* a low slope in voltage vs. time. Also, in dark exposures, they integrate a dark current that is consistent with the mean dark current on the array. The low raw signal and dark current make sense since the reset transistor can still communicate with the pixel in the multiplexer even if it is not connected to the detector material via the indium bump bond, and the pixel can still integrate leakage currents from the ROIC.

The most likely explanation for this behavior is that the  $p^+$  implant of an open pixel in the detector PIN diode has some varying degree of impedance to the silicon in the multiplexer. The actual potential in the implant may be very high—perhaps close to  $V_{SUB}$ —so that lateral diffusion is taking place at the front surface of the detector (see Section 6.1.4.3) and causing the potential in the neighboring pixels to increase. But because of the high impedance, there is some voltage drop between the  $p^+$  implant and the  $p^+$  silicon in the multiplexer for the open pixels.

### 4.2.4 Volcanoes

In certain areas of the HyViSI detectors there are groups of hot pixels clustered together. When the voltage in these pixel reaches the upper rail, it appears that the charge spills over into the neighboring pixels. When these neighboring pixels have sufficient charge, the spilling proceeds to

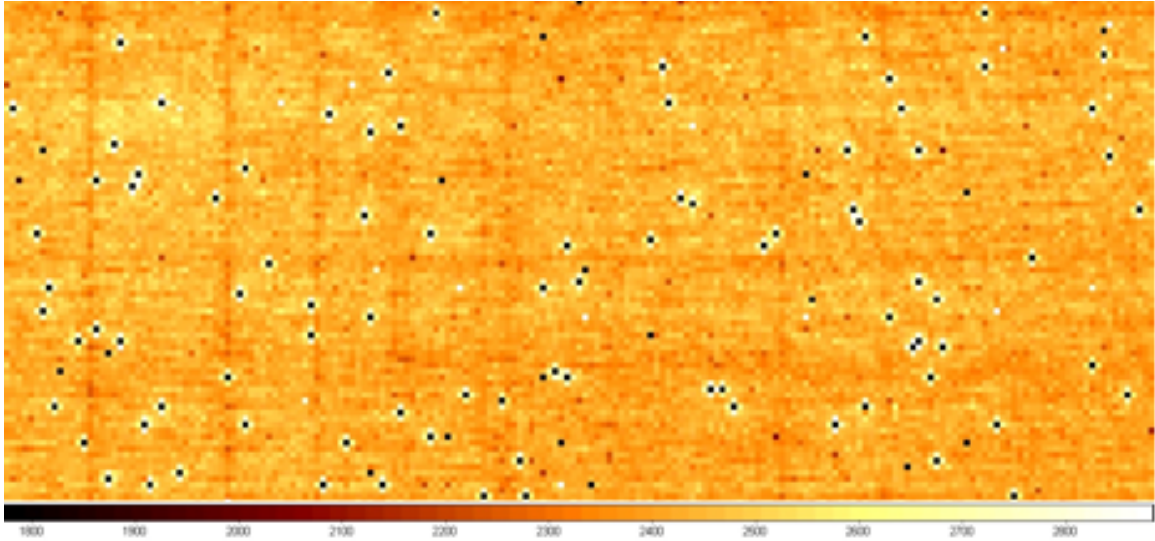


Figure 4.2: Difference image of portion of H4RG-10-007 array under flat field illumination at 1000 nm. Notice that there are two populations of dark pixels. One is surrounded by neighbors with normal response and another is surrounded by pixels with elevated apparent response. The former are identified as hot pixels which have a difference near zero and the latter are identified as open pixels.

their neighbors, and so on. For this reason, they have been dubbed “volcanoes”. The pixels in these clusters are classified as either dead or hot, so their numbers are included in those categories.

#### 4.2.5 Summary of Pixels

The summary of the unusable pixels for the principle detectors tested in this thesis is tabulated in Table 4.2. H4RG-10-007 has an inordinately large number of high dark current pixels in addition to a high mean pixel dark current. This problem was linked to an anti-blooming diode in the multiplexer and has been removed in the new pixel architecture (Yibin Bai, Private Communication).

Table 4.2: Pixel Type Fractions for HyViSI Detectors Tested

Detector	Dead		Open		Hot		Total	
	#	%	#	%	#	%	#	%
H4RG-10-007	6341	0.0378%	76,959	0.4587%	210,063	1.2520%	293,363	1.7486%
H2RG-32-147	197	0.0047%	293	0.0070%	1528	0.0364%	2018	0.0481%
H1RG-022	7	0.0007%	52	0.0050%	44	0.0042%	103	0.0098%

### 4.3 Conversion Gain and Nodal Capacitance

One of the most important properties of any detector is the net conversion gain between the digital number (DN or ADU) recorded for a pixel and the amount of charge present in the collecting node of that pixel.<sup>1</sup> We shall call this gain  $G_{NET}$  since it represents the product of all gain stages in the signal path between the physical charge in the pixel and the DN recorded in the DAQ. Nearly all of the other detector properties such as read noise, quantum efficiency (QE), etc. rely on this measurement. In addition, when combined with the QE, it can provide an estimate of the apparent magnitude of astronomical sources when photometric standards are not available.

#### 4.3.1 Contributions to the Gain

$G_{NET}$ , measured in  $e^-/\text{ADU}$ , is the product of several gain stages:

$$G_{NET} = G_{PIXEL} * G_{UC} * G_{OUT} * G_{AMP} * G_{A/D} \quad (4.3)$$

The pixel gain,  $G_{PIXEL}$  ( $e^-/\text{V}$ ), accounts for the voltage change per unit charge, also known as the inverse of the capacitance. It is linear over small signal ranges but becomes nonlinear when the pixel is near capacity. The detector readout has two source follower FETs between each pixel and the output pad. One is in each unit cell, and it induces a gain of  $G_{UC}$  (V/V). The other, the output FET, introduces a similar gain, referred to as  $G_{OUT}$  (V/V). The output FET may or may not be included in the signal path, but for this discussion it is assumed to be. The processing electronics have stages to amplify the signal, and this amplification is included in the term  $G_{AMP}$  (V/V). Finally,  $G_{A/D}$  (V/ADU), represents the conversion between volts and analog to digital units (ADUs). In the case of the SIDECAR and ARC electronics, we can express the product of the latter two gains as the electronics gain,  $G_{ELEC} = G_{AMP} * G_{A/D}$ .

In the following sections we shall describe each of these gains in a little more detail, along with the methods by which they are measured.

#### 4.3.2 Electronics Gain – $G_{AMP}$ & $G_{A/D}$

Measuring the conversion gain of the SIDECAR ASIC control electronics was described in Section 3.5.2. The same technique, applicable to any A/D converter and amplification stage, was also applied to the ARC controller.

Both sets of electronics allow the signal to bypass the amplification stage and go directly to the A/D. Making the measurement in this configuration will yield  $G_{A/D}$  (V/ADU). Including the amplification stage and repeating the measurement will yield  $G_{ELEC} = G_{AMP} * G_{A/D}$ , from which

---

<sup>1</sup>The term *node* may be used interchangeably with pixel in this case.

$G_{AMP}$  (V/V) can be inferred. We did not bypass the preamp of the SIDECAR while collecting science data because it aids in filtering and buffering the signal to the A/D.

### 4.3.3 Unit Cell Source Follower Gain – $G_{UC}$

Each unit cell of the HxRG multiplexers contains a FET source follower (SF) that buffers the voltage present at its gate to the detector output. In the case of the HyViSI devices, this voltage,  $V_{node}$ , is generated by the charge contained in the  $p^+$  implant of the photodiode. The voltage at the source of the FET will follow the voltage at the gate amplified by a gain,  $G_{UC}$ , that is less than unity. The gain of the FETs is sometimes referred to as the *electronic gain* of the detector.

As shown in Figure 4.3, the gate of the unit cell SF can be held at the potential  $V_{reset}$  while the reset switch in the pixel is closed. If the output FET at the right of the figure is bypassed by closing the switch controlled by BUFDISABLE, we can directly measure a change in voltage at the output,  $\Delta V_{OUT\ NOSF}$ , induced by a change of  $\Delta V_{RESET}$ . The two are related by:

$$\Delta V_{OUT\ NOSF} = \Delta V_{RESET} * G_{UC} * G_{ELEC}. \quad (4.4)$$

To obtain  $G_{UC}$  we program a set of voltages for  $V_{RESET}$  using the control electronics and measure the corresponding values of  $V_{OUT\ NOSF}$ . When we plot the quantities, the slope gives us  $G_{UC}$ .

### 4.3.4 Output Source Follower Gain – $G_{OUT}$

The method for measuring  $G_{OUT}$  is nearly identical to the one described for measuring  $G_{UC}$  except that we close the switch controlled by BUFDISABLE, thereby placing the output SF in the signal

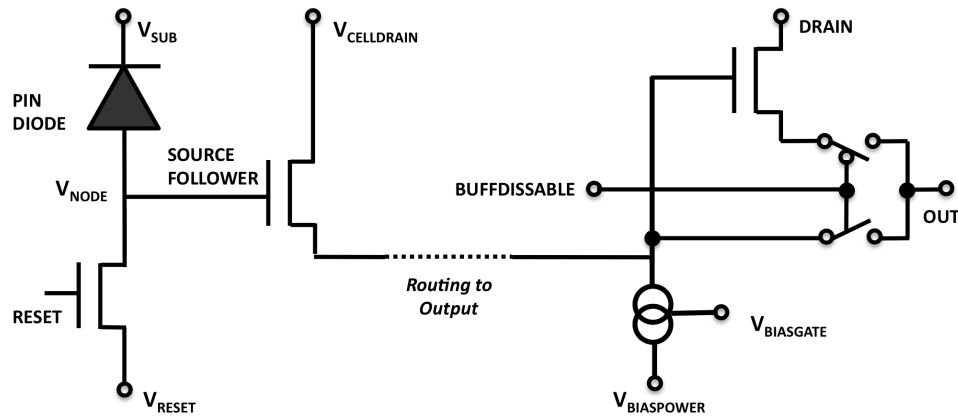


Figure 4.3: A diagram showing the unit cell, control lines, and routing at the output of the detector. Two source followers are present in the signal path with gains  $G_{UC}$  and  $G_{OUT}$ .

path. With both FETs contributing gain, Equation 4.4 becomes

$$\Delta V_{OUT\ SF} = \Delta V_{RESET} * G_{UC} * G_{SF} * G_{ELEC}. \quad (4.5)$$

Since  $G_{UC}$  is known, we can solve for  $G_{SF}$ . In Figure 4.4, we show the DN (given by  $DN = V_{OUT\ SF}/G_{ELEC}$ ) vs.  $V_{RESET}$  for H1RG-022. This data was taken with both FETs active so the slope of the line is  $G_{UC} * G_{SF}$ . It should be noted that both of these gains are heavily dependent on the current available to their respective FETs. The gain and linearity of the pixel source follower will increase with decreasing  $V_{BIASGATE}$ , since decreasing this voltage increases the drain current of the unit cell FET. For the output FETs, these quantities will depend similarly on the current supplied to them through either a pull-up resistor or current source external to the detector.

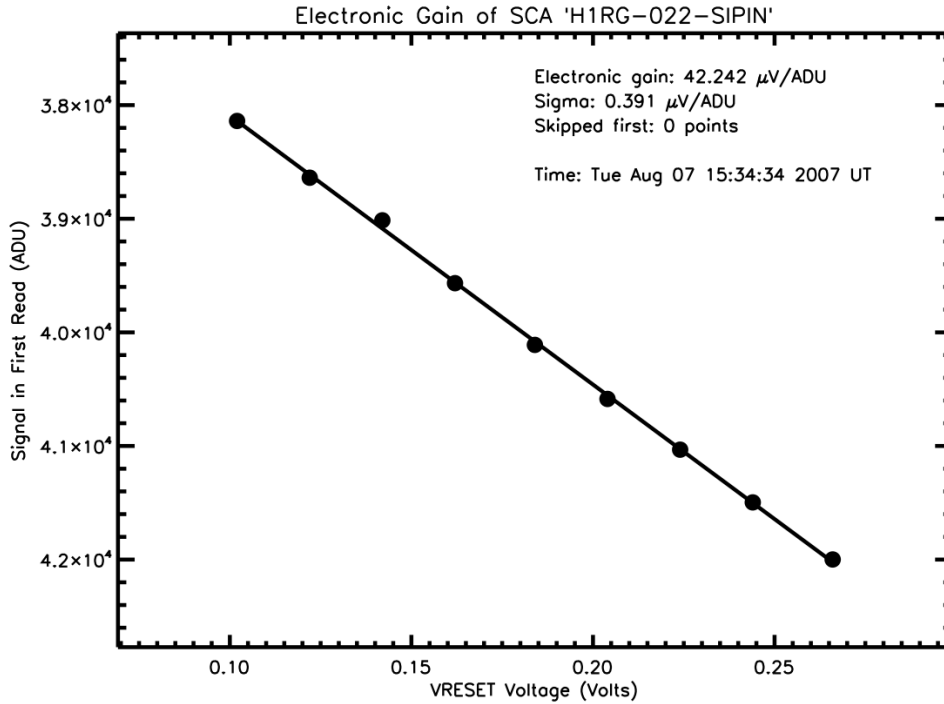


Figure 4.4: DN vs.  $V_{RESET}$  measured while the pixel reset is held down. The slope of this line is used to determine the gain of the unit cell SF and the output SF.

### 4.3.5 Net Conversion Gain – $G_{NET}$

Several methods can be used to obtain the number of electrons needed to change the ADU count by one. They include noise squared vs. signal (photon transfer),  $\text{Fe}^{55}$  calibration, and the capacitance comparison method. For Hybrid CMOS arrays, it has been shown that the noise squared vs. signal method overestimates the nodal capacitance and, in turn, the conversion gain [52]. To avoid this, we use the  $\text{Fe}^{55}$  method to estimate the conversion gain and the average pixel capacitance.

#### 4.3.5.1 $\text{Fe}^{55}$ Test

$\text{Fe}^{55}$  is a radioactive material that is commonly used in astronomy to calibrate detectors in both space and ground based missions. An  $\text{Fe}^{55}$  atom produces soft x-ray photons when it decays into an Mn atom, and the energy spectrum of these x-rays and their interaction behavior in silicon is well known [3]. The five most prominent emission lines and the number of electrons they will produce upon interacting in a silicon substrate (assuming that  $3.65 e^-/eV$  are produced) are listed in Table 4.3.

Table 4.3:  $\text{Fe}^{55}$  lines along with the number of electrons they generate in Si. The process that generates the photon, where  $\rightarrow$  indicates an electron moving from one orbital shell to another, is also indicated.

Line	Energy (keV)	Number of $e^-$	Process
$K_\alpha$	5.9	1620	L $\rightarrow$ K Shell with Auger Process
$K_\alpha$ escape	4.2	1133	L $\rightarrow$ K Shell
$K_\beta$	6.5	1778	M $\rightarrow$ K Shell with Auger Process
$K_\beta$ escape	4.8	1291	M $\rightarrow$ K Shell
Si	1.7	487	Photon Escapes

The  $K_\alpha$  line is significantly stronger than the other lines. It is emitted 7 times more frequently than the  $K_\beta$  line, which is the next in order of strength. The  $\text{Fe}^{55}$  test is sometimes referred to as the “acid test” for imagers [11] because a detector that has poor charge collection efficiency (CCE), read noise, CTE, QE, or any combination of these will not be able to distinguish between these separate peaks. Instead, the distribution of counts due to  $\text{Fe}^{55}$  hits will appear broadened spectrum that peaks around the  $K_\alpha$  line.

$\text{Fe}^{55}$  sources are fairly easy to come by, small in size, and relatively inexpensive, making them a good calibration tool for astronomy. One position in the filter wheel contained inside the RIDL dewar held an  $\text{Fe}^{55}$  source to calibrate each of the HyViSI devices. With the source available at any time, we were able to use it before each telescope observing run and verify the conversion gain of the detector being used. In the dewar used at Teledyne Scientific, the source had to be inserted

and removed by hand, but resulted in approximately the same configuration as the one in the RIDL system.

To measure the conversion gain with the  $\text{Fe}^{55}$  source we obtain a large number of exposures while the  $\text{Fe}^{55}$  source is located an inch above the detector. In collecting the data, we switch between CDS window mode with a small window size and full frame up the ramp mode. The former method better avoids double hits in a single read, which makes data analysis easier. It also provides better time resolution on the signal in each pixel. However, it severely diminishes the collection area, and thus, the effective hit rate in comparison to full frame mode.

Once all the data have been collected, they are analyzed to find single pixel events according to the method described in Section 6.1.3. We histogram the data and assume the peak in ADU corresponds to  $1620 e^-$ . An example histogram for H2RG-32-147 is shown in Figure 4.5.

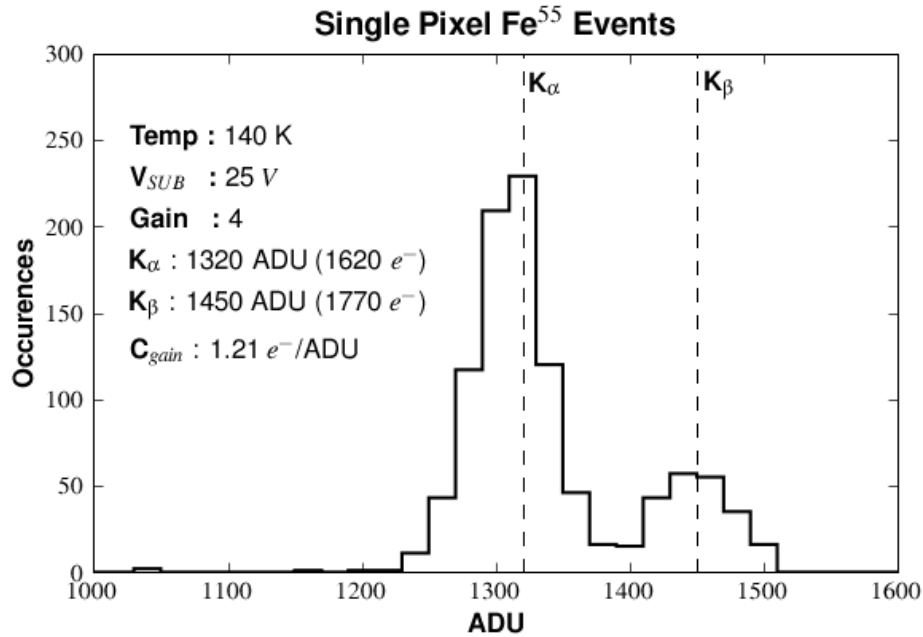


Figure 4.5: Histogram of single pixel events while the detector H2RG-001 was exposed to the Iron 55 source. The data was collected in window mode with a frame time of 1.6 seconds. Operating parameters are listed. The  $K_\alpha$  and  $K_\beta$  peaks are clearly discernible, indicating good energy resolution.

#### 4.3.6 Nodal Capacitance – $G_{PIXEL}$

$G_{PIXEL}$  is effectively the nodal capacitance,  $C_{NODE}$ . It is a very important quantity that is often a steering factor in the fabrication of the detector. Unfortunately, it is a double edged sword in a way. If  $C_{NODE}$  is too small the pixel will not be able to hold much charge, and this will result in a small

dynamic range. In other words, the pixels will saturate very quickly. Due to the dependence on the area of the pixel, nodal capacitances are getting smaller as advances in CMOS processing yield smaller pixel dimensions. If  $C_{NODE}$  is too large, on the other hand, an electron added to the pixel will change the voltage of the node by a negligible amount. It will thus take a significant amount of electrons to increase the DN by one, resulting in poor sensitivity. Ultimately, a compromise is sought that will result in both good dynamic range and sensitivity.

With all of the quantities  $G_{NET}$ ,  $G_{UC}$ ,  $G_{SF}$ ,  $G_{A/D}$ , and  $G_{AMP}$  in hand, Equation 4.3 can be inverted to find  $G_{PIXEL}$ . What we actually calculate is not just the capacitance of the PIN photodiode, but rather the sum of capacitances referred to as  $C_{total}$  in Section 2.2.2.

### 4.3.7 Results for HyViSI Detectors

Table 4.4 shows an example of the individually measured gains for H4RG-10-007. The product  $G_{UC} * G_{OUT}$  was found to be very low relative to the value of 0.90 that is typically measured in hybrid CMOS arrays. For the other HyViSI devices, only  $G_{NET}$  was measured specifically. Values for  $G_{PIXEL}$  of these devices were estimated using  $G_{UC} * G_{OUT}=0.9$  and are listed along with the well depth in Section 4.7.

Table 4.4: Measured gains using the ARC electronics and the H4RG-10-007 Si PIN detector

H4RG LEACH SFE					
$G_{NET}$	$G_{AMP}$	$G_{A/D}$	$G_{UC} * G_{OUT}$	$1/G_{PIXEL}$	Unit Cell Capacitance
( $e^-/ADU$ )	(V/V)	( $\mu V/ADU$ )	(V/V)	( $\mu V/e^-$ )	(fF)
2.32	1.81	42.97	0.736	25.21	6.347
0.63	6.62	11.08	0.725	24.45	6.544

#### 4.3.7.1 Dependence of Conversion Gain on Temperature

The drain current of the pixel source follower decreases with decreasing temperature if the voltage to its current source,  $V_{BIASGATE}$ , is held constant. This decrease in current will translate into a loss of gain—less  $\mu V/e^-$  and thus, less  $ADU/e^-$ —for the pixel, as well as a decreased transconductance. The impact of the decreased transconductance on noise will be discussed later in Section 4.4.1.2. The impact on the conversion gain  $G_{NET}$  is shown in Figure 4.6. As expected, the conversion gain decreases with decreasing temperature. To prevent this from happening, the voltage  $V_{BIASGATE}$  must be adjusted accordingly.

Figure 4.6 also shows an unexpected and not yet understood effect that was observed several times during temperature cycling and testing of H2RG-001. On four separate occasions, a very large

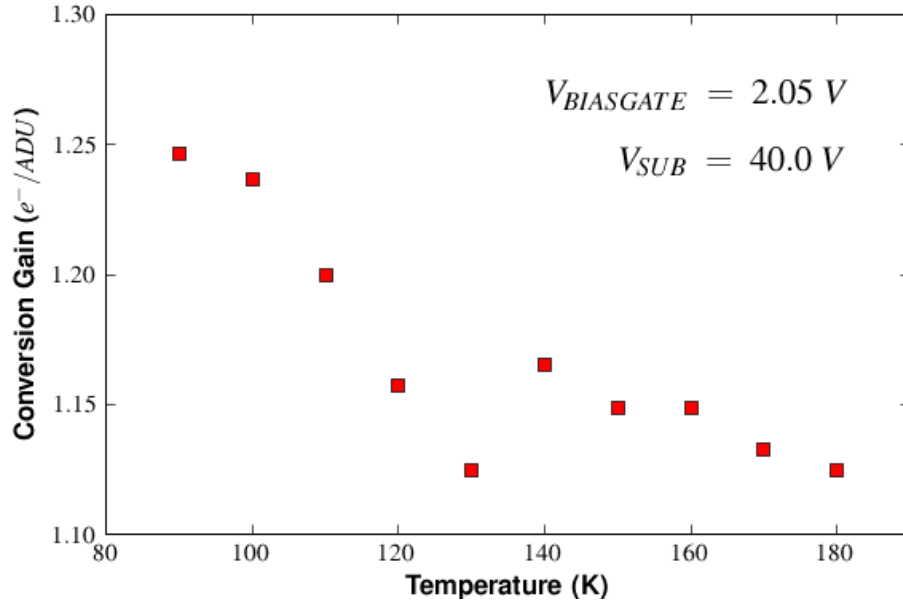


Figure 4.6: With the voltage to the pixel source follower current source  $V_{BIASGATE}$  held constant, the net conversion gain is seen to decrease with decreasing temperature. The discontinuity at 140 K is related to an unexplained shift in signal for all detector outputs that occurred several times when using H2RG-001.

voltage spike was seen after the detector was warmed to 130 K or 140 K. In each case, the voltage spike occurred during up-the-ramp integrations and lasted less than 10 seconds. After the spike, the average output signal increased by about 120 mV for all science pixels on the array and by about 100 mV for the reference pixels. A decreased read noise was observed after the spike, along with a rise in  $G_{NET}$ . The effect was only observed when the substrate voltage was greater than 10 volts, which might seem to suggest that it is related to a shift in the equilibrium state of carriers in the bulk. However, because it was also observed in the reference pixels, which do not see the substrate voltage, this cannot be the case. The most plausible culprit seems to be the protection diode circuitry for  $V_{SUB}$ . It is not known whether this circuitry is located in the cryogenic SIDECAR readout electronics or on the pads of the readout multiplexer.

## 4.4 Read Noise

Any image produced by a detector can be divided into two components: *signal* and *noise*. The signal is the part that we are interested in; it represents the imprint of the incoming light on the detector. The noise is the part that we wish to get rid of or minimize. Some of the noise is inherent in the light itself and physically inevitable. Photons have a shot noise associated with them, which means the more photons that fall on the detector in a given time, the larger the spread in their number will be. The other portion of noise is related to the way in which the photons are converted into a measurable signal, and the electronics used to detect the signal, including everything from the uncertainty of charge on a capacitor to fluctuations in the number of electrons that actually make it through the drain of a transistor. This is the portion that we seek to eliminate with improvements in detector technology. In astronomy, a low read noise is absolutely critical for faint source detection.

### 4.4.1 Sources of Read Noise in Hybrid CMOS Detectors

Noise sources in CMOS detectors have been studied and modeled extensively. It is beyond the scope of this thesis to treat these sources in detail. However, basic descriptions of the most dominant noise sources in Hybrid CMOS detectors are given in the following sections and the reader is pointed to the references that provide exhaustive detail.

#### 4.4.1.1 kTC Noise

At the simplest level, resetting the pixels in a hybrid CMOS detector can be viewed as filling or draining a capacitor of charge through a resistive path [66]. The resistive path is the channel of the reset MOSFET transistor and the capacitor is the capacitance of the pixel node, as shown in Figure 4.7. During reset, the transistor is in its “On” state and current flows through the channel against

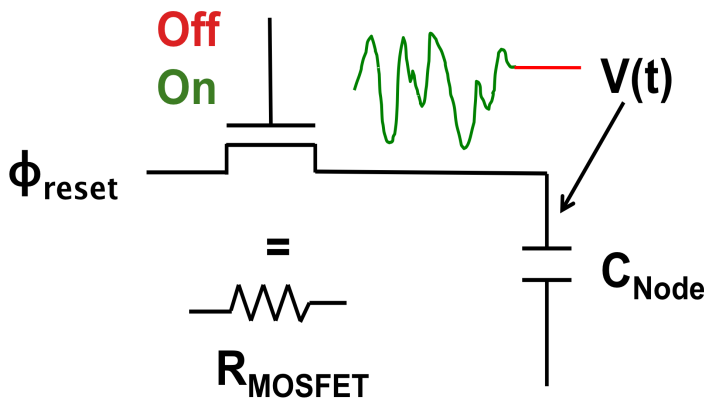


Figure 4.7: A very simple illustration of the process that generates reset noise in CMOS pixels. While the reset switch is closed, thermal Johnson noise causes the voltage  $V_{\text{Node}}$  to oscillate, as shown by the green line. When it is opened, the impedance of the switch is ideally high enough to prevent any current from flowing, leaving the voltage at the level shown by the red line.

an effective resistance  $R_{MOSFET}$ . The voltage, and thus the charge, at the pixel node fluctuates due to thermal Johnson noise inherent in the current flow. When the switch is finally opened and the transistor is turned “Off”, the high impedance of the channel fixes the node voltage at whatever level it was at during the oscillations,  $\phi_{reset}$ . And since this circuit is essentially a low pass filter with an equivalent noise bandwidth of  $B = 1/(4R_{MOSFET}C_{Node})$ , the RMS of the distribution of voltage and charge that will be measured in a large sample can be shown to be [3]

$$\sigma_{kTC}(V) = \sqrt{\frac{kT}{C_{Node}}} \quad \sigma_{kTC}(e^-) = \sqrt{\frac{kTC_{Node}}{q}}, \quad (4.6)$$

where  $k$  is Boltzmann’s constant.

With a capacitance of  $C_{Node} = 14\text{fF}$ , the reset noise is very substantial in HyViSI detectors. At 180 K, it is about  $40\text{ e}^-$  and at 130 K, it is about  $33\text{ e}^-$ . At a level of  $30+\text{ e}^-$ , it may well dominate all other sources. Removing it with a correlated double sample (CDS) or any one of the methods described below is essential in scientific applications.

#### 4.4.1.2 Source Follower Noise

Similar to the output amplifier in a CCD, the transistors in the CMOS multiplexer contribute noise to the signal measurement during a read. Janesick provides an excellent, thorough description of the noise sources associated with MOSFETs: white noise, flicker or  $1/f$  noise, shot noise, contact noise, and popcorn noise [3]. While all the FETs in the multiplexer may contribute noise, several authors point out that the main noise contributor to read noise in the CMOS signal path is the pixel source follower [67, 68, 69]. The spectrum of the pixel source follower noise is generally dominated by a “white” and “pink” component.

**White Noise** White noise is random and has a flat power spectral density. The exact expressions in the references [67, 68, 69] for the white thermal noise voltage at the source of the transistor varies depending on the geometry considered, but they share in common the form:

$$\bar{V}_n^2 \propto \frac{kT}{Cg_m}, \quad (4.7)$$

where  $k$  is Boltzmann’s Constant,  $T$  is the temperature,  $C$  is a term representing the effective capacitance of the regions downstream of the transistor source, and  $g_m$  is the transconductance of the transistor. As Moore points out [43], since the transconductance goes like the square root of the drain current, a high drain current should be used for the pixel source follower to achieve low noise. For the HxRG multiplexers, the drain current is controlled by the bias voltage  $V_{BIASGATE}$ . It is indeed found that by lowering this voltage (which increases the drain current) the signal amplitude increases and the noise decreases. And since the current decreases with decreasing temperature, it

is important to adjust  $V_{BIASGATE}$  when changing the detector temperature.

**Pink Noise** Pink noise is characterized by a power spectral density that grows with decreasing frequency  $f$ , with a dependence  $\propto 1/f$ . It is often called “one over f noise” or “flicker noise”. For MOSFETS, its origin is believed to lie in the trapping of current carriers while they flow through the transistor channel [3]. When large numbers of electrons are trapped and de-trapped, the current is modulated, resulting in a noise that shows the  $1/f$  shape. Large area devices are well described by classical  $1/f$  noise models that assume large numbers of carriers, but for smaller devices, these models break down because the number of mobile charge carriers is small and behavior of individual charge carriers becomes visible and significant [70]. In this *Random Telegraph Signal (RTS)* regime, the presence of even one individual trap may be observed as noise that looks like a toggling between an “on” and “off” state in the output signal. Expressions for  $1/f$  and RTS noise are given in [3, 14, 70].

#### 4.4.1.3 Dark Current and Photon Shot Noise

It is well known that both dark current and photons exhibit *Poisson* noise, commonly referred to as shot noise. Simply stated in the context of detectors, if the dark current or photo current produces an average of  $N$  electrons in a time  $t$ , then the variance in the number of electrons produced will also be  $N$  in that same time for a set of measurements. Consequently, the noise will be higher for high luminosity measurements, where  $N_{photons}$  is high, and high temperatures, where  $N_{dark}$  is high.

#### 4.4.1.4 Bias Coupling Noise

Noise in the voltages and currents used to bias the detector can couple to the pixel node and output bus, creating another source of noise in measurements of pixel values. For instance, an oscillating  $V_{BIASGATE}$  will cause the drain current in the pixel source followers to shift as well, which translates to an oscillating output voltage, independent of what pixel is being sampled. Moore finds evidence that the row enable FET and reset FET couple to the pixel node voltage [43]. Noise in either of these transistors will translate into noise in the pixel.

#### 4.4.1.5 Output Crosstalk Noise

When multiple outputs are being used on the HyViSI detectors, a large signal on one output will couple to the other outputs. Evidence for this will be shown in Section 6.2. In addition to systematically raising the signal on the other outputs, noise on the high voltage being transmitted as well as the shot noise on the electrical current that carries the high signal will present itself on the other outputs.

## 4.4.2 Noise Reduction Techniques

The HxRG reference pixels and separate reference output can both be used to eliminate common mode noise. The application of the reference pixels, which were described in Section 3.4, are discussed later in Section 5.2.2 and the separate reference output is covered below. Aside from these, the unit cell and readout multiplexer of the HyViSI possess no circuitry to remove noise in the analog domain. However, in the digital domain, correlated  $kTC$  reset noise can be eliminated and uncorrelated noise can be diminished by reading the pixel multiple times and properly manipulating the values. Techniques to manipulate the pixel values are well treated in Fowler et al. [71]. The three most common of these: Correlated Double Sampling, Fowler Sampling, and Slope Fitting, are discussed below. All of the techniques described are hinged on the non-destructive readout of the hybrid pixels.

### 4.4.2.1 Common Mode Referencing

Perhaps the single most useful signal delivered by the multiplexer is the reference output  $V_{REFOUT}$ . This is an independent output channel derived from a single pixel, which is connected to either  $D_{SUB}$  or  $V_{RESET}$ , and is read out in parallel with the other pixels. Any common mode noise introduced by the power supply, picked up as interference, etc. can be eliminated by using this voltage as the reference for the video outputs. As a demonstration of its importance, with all other aspects of our test system configuration being equal at  $T = 100$  K, the RMS read noise drops from  $40 e^-$  CDS when referencing the detector outputs against  $V_{REFMAIN}$  to  $10 e^-$  CDS when referencing against  $V_{REFOUT}$ .

Great care should be taken to ensure that  $REFOUT$  is wired correctly to the control electronics for differential analog measurement. For instance, if it is wired to inputs  $InP32 - InP36$  on the SIDECAR, one is forced to sample both it and the video signal against an internal SIDECAR reference, and subtract the two signals digitally. Since the electronics noise in the two channels is uncorrelated, an additional noise factor of  $\sqrt{2}$  will be introduced. On the other hand, if  $V_{REFOUT}$  is wired to  $InPCommon$ , the input routing multiplexer can be used to feed it to the negative side of the preamp in every channel, allowing a truly analog differential measurement.

### 4.4.2.2 Correlated Double Sampling

Correlated Double Sampling (CDS) is the most easily understood and implemented multiple sampling technique. CDS is a widespread technique in astronomical imaging, and it should be emphasized that the CDS technique described here is a *digital* one and not an *analog* CDS like the one used in the output amplifier of a CCD. To obtain a digital CDS, after resetting a pixel at  $i, j$ , the pixel is read once at time  $t_1$  and then again at  $t_1 + \Delta t$ , yielding the values  $S(i, j, t = t_1)$  and

$S(i, j, t = t_1 + \Delta t)$ . The signal is then calculated as:

$$S(i, j) = \frac{S(i, j, t = t_1 + \Delta t) - S(i, j, t = t_1)}{\Delta t}. \quad (4.8)$$

Note that no restriction is placed on the sampling pattern. The pixel at  $i, j$  can be read twice in succession before clocking to the next pixel or all pixels in the frame can be read before returning to  $i, j$ ; the difference is accounted for by  $\Delta t$ . Figure 4.8 can be used to visualize the second of these sequences if  $N_{Fowler} = 1$  and  $t_{FowlerExp} = \Delta t$ .

CDS eliminates  $kTC$  noise and has been speculated to improve spatial uniformity [71]. It is straightforward to deduce that the  $1/f$  component noise component will depend on the integration time. If the detector is read noise limited, CDS will be bested by a technique that uses more than two samples. But interestingly, if the detector is background limited<sup>2</sup>, CDS will yield the best estimate of the signal. Garnett and Forrest provide an elegant proof of this in [72].

#### 4.4.2.3 Fowler Sampling

Multiple Correlated sampling, or Fowler sampling, named for its pioneer Al Fowler, is a technique that was first implemented in infrared arrays to reduce read noise [71]. In a Fowler sampling sequence,  $N_{Fowler}$  reads of the detector are performed immediately after the pixels are reset. Then, after some integration time  $\Delta t = t_{FowlerExp} + t_{FowlerPair}$ ,  $N_{Fowler}$  more reads are taken. The signal estimate is given by:

$$S(i, j) = \frac{\sum_{r=N_{Fowler}+1}^{2N_{Fowler}} S(i, j, r) - \sum_{r=1}^{N_{Fowler}} S(i, j, r)}{N_{Fowler} \Delta t}. \quad (4.9)$$

Figure 4.8 shows a Fowler sequence with  $N_{Fowler} = 5$ . Often times, such a sequence is referred to as *Fowler 5*, or Fowler sampling with *5 Fowler Pairs*, since each of the reads in the first set is matched with another in the second.

If the noise in each read  $\sigma_r$  is white, then the effective noise for the signal estimate given in Equation 4.9 will be [73]:

$$\sigma_t = \sqrt{\frac{2}{N_{Fowler}}} \sigma_r. \quad (4.10)$$

This equation can also be applied to the CDS case, where  $N_{Fowler} = 1$ . Garnett and Forrest show that Fowler Sampling achieves its best performance at a duty cycle of  $2/3$ , meaning that  $2/3$  of the total observing time is spent sampling the pixels [72]. In the context of Figure 4.8 this means  $t_{FowlerPair} = t_{FowlerExp}$ . Even with the optimum duty cycle, though, Fowler Sampling yields a slightly worse signal-to-noise (SNR) ratio than Slope Fitting (by about  $\sim 6\%$ ). Also, if used in a

<sup>2</sup>Signal to noise calculations are often divided into two regimes. *Read-noise limited* is the case where the detector noise is dominated by the readout process. *Background limited* or *shot-noise limited* is when the detector noise is dominated by photon shot noise.

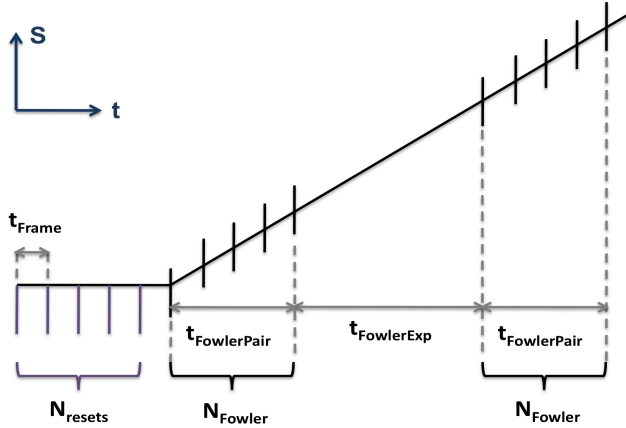


Figure 4.8: A diagram showing an up the ramp exposure with Fowler Sampling. Before the exposure,  $N_{resets} = 5$  resets are performed. At the front of the integration,  $N_{Fowler} = 5$  samples are taken. After a wait time of  $t_{FowlerExp}$ , another 5 samples are taken. It should be noted that during the wait time, the detector should still be clocked to avoid thermal instability.

manner in which only the final value  $S(i, j)$  is saved to disk, Fowler Sampling offers no means to reject cosmic ray events. In fact, Offenberget al. [73] show that the SNR is reduced to zero at the locations hit by cosmic rays. If all of the samples are saved, however, an estimate for  $S$  can still be obtained by only considering certain reads.

It is worth mentioning that the real benefit of the Fowler method is the simplicity of the algorithm and the small amount of data storage required. The astute reader might also gather that a reduction in electrical power can be gained by leaving the detector idle during the period of time  $t_{FowlerExp}$ , and this would be correct for an ideal detector. However, when the HyViSI pixels are not clocked during this period, a large offset in signal is observed for the second set of reads even with no illumination. The sign and amplitude of the offset are not understood and the latter can vary greatly depending on the operating conditions. For this reason, the pixels must be clocked in the same fashion as they are during the sampling period and no power will be saved.

#### 4.4.2.4 Slope Fitting

As an alternative to simply averaging reads and subtracting pairs, a straight line can be fit to the signal as a function of time. The slope of the line yields an estimate of the instantaneous photocurrent in the pixels, and thus the flux  $F$ . This method is referred to as *Slope Fitting* or *Sampling-Up-The-Ramp (SUR)*. It reduces both  $1/f$  and white noise, and is very useful in detecting large jumps or dips in signal due to cosmic rays, voltage spikes, and “noise bursts” [74]. It is computationally intensive, however, and difficult to implement in FPGAs and control electronics circuitry. As mentioned in the previous section, it does offer slightly better performance than Fowler Sampling in the read-noise limited case. If  $N$  equally spaced samples are used for the fit with equal weighting of each, then the effective noise will be [75]:

$$\sigma_t = \sqrt{\frac{12}{N}} \sigma_r. \quad (4.11)$$

Note that the duty cycle and integration time of a Fowler Sampling scheme must be taken into account when comparing Equations 4.11 and 4.10. The exact implementation of this method will be covered in Section 5.2.4 in the context of astronomical data reduction.

### 4.4.3 HyViSI Measurements

There are several standard practices for measuring read noise in hybrid detectors [76]. In the *temporal* method, a stack of CDS frames are collected and the RMS value for each pixel across the frames is computed to form a final two-dimensional image. The pixel values thus indicate how the signal in a given pixel varies over time, and the mean of the RMS values is the figure that is reported as an estimate of the variation. In the *spatial* method, also referred to as the *pixel-to-pixel* method, two CDS frames are subtracted from each other and the resultant frame is divided by  $\sqrt{2}$  to account for the statistical increase in noise due to subtraction. The resulting **read noise map**, an example of which is shown on the left in Figure 4.9, is then binned into a histogram after significant outliers have been rejected. The histogram is then fit with a Gaussian to yield a standard deviation and RMS value for the distribution.

As mentioned previously, spatial read noise measurements for H1RG-022, H2RG-32-147, and H4RG-10-007 were dominated by noise from the reference voltage on the JADE card and showed excessively high noise (20-40  $e^-$ ). The spatial read noise values obtained for H2RG-001 were the best obtained and ranged from 7-13  $e^-$  RMS. As Figure 4.9 shows, the noise floor is dominated by a pattern that shows up as strong banding and has a power spectrum characteristic of  $1/f$  noise.

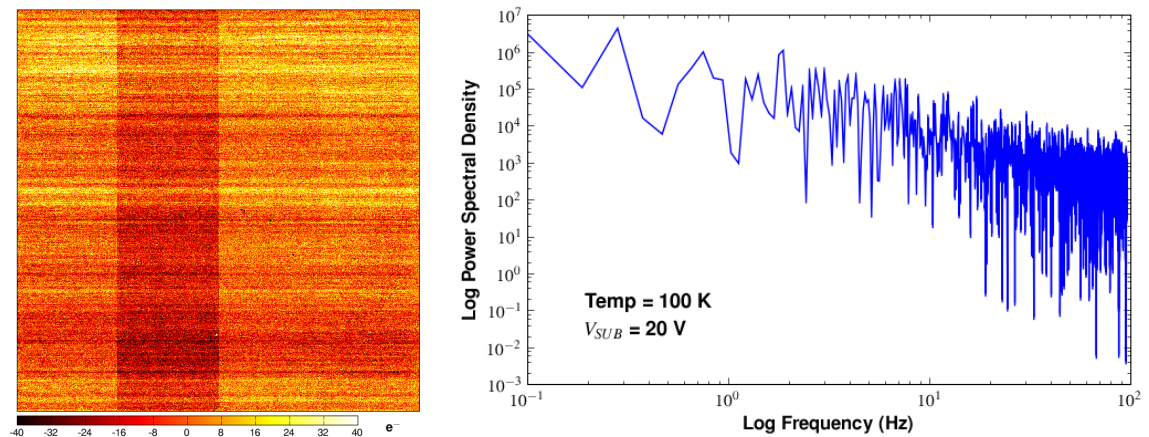


Figure 4.9: (Left) Read noise map of H2RG-001 at 100 Kelvin operated with four outputs. Each of the four outputs was averaged on eight channels in the SIDECAR, and the preamps in the SIDECAR were only reset once per frame. (Right) The power spectrum shows that the strong banding is dominated by  $1/f$  noise, which sets the noise floor.

Note that the horizontal structure is not the same as the row-to-row reset noise of the SIDECAR preamps described in Section 3.5.1. If it were the latter, each of the four channels for the detector would have its own independent banding pattern. In fact, for these measurements the SIDECAR preamps were reset only once per frame and each of the four detector outputs were averaged on eight SIDECAR channels. Numerous attempts to reduce the  $1/f$  banding with grounding measures and voltage and current adjustments on the SIDECAR were unsuccessful. However, after subtraction of the reference pixel columns, the banding is greatly reduced. And subtracting the mean of the reference pixels for each channel eliminates the channel to channel offsets, as shown in the read noise map of Figure 4.10.

Figure 4.10 also shows the measured CDS read noise for H2RG-001 as a function of temperature with the backside contact voltage at 25 volts. The measurements were made with the detector operating in window mode with a frame time of  $t_{frame} = 10.6$ s and a window size of 300x300 pixels. Interestingly, the noise decreases with increasing temperature until it hits a minimum at 130-140 K and then increases thereafter. One possible explanation for this is that the transconductance of the pixel source follower was decreasing for  $T < 130$ K as a result of a constant  $V_{BIASGATE}$ . The constant  $V_{BIASGATE}$  causes a decrease in the drain current, which in turn increases the noise. For temperatures above 140 K, the increase in noise is assumed to be a result of increased thermal noise, although the slope is not linear.

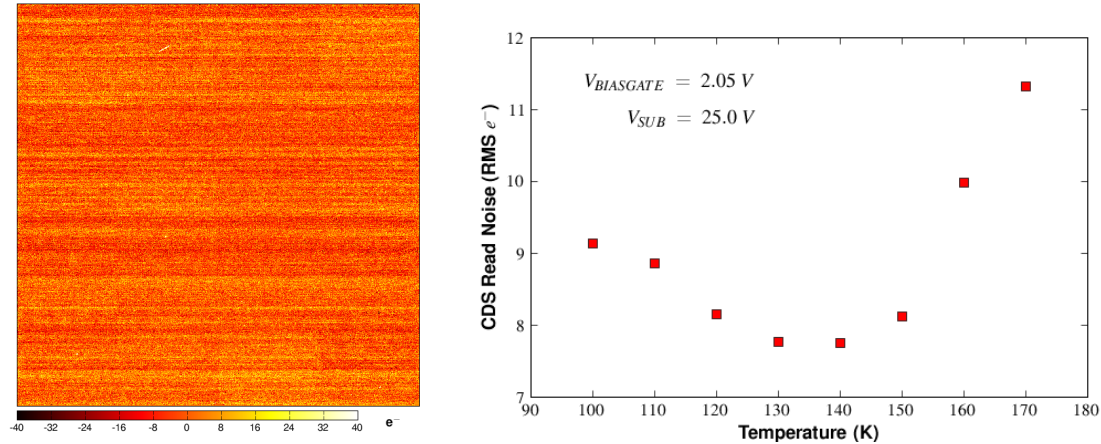


Figure 4.10: (Left) Read noise map of H2RG at 100 Kelvin operated with four outputs after reference pixel correction. (Right) Read noise vs. temperature for H2RG-001. The increase of read noise at low temperatures is due to the decrease in transconductance of the unit cell source follower and the increase at high temperatures is a result of increasing thermal white noise.

The read noise improves slightly at 40 volts, as shown in Figure 4.11, and there is evidence that it will continue to decrease with increasing  $V_{SUB}$  [40]. In addition to the temperature dependence for CDS ( $N_{FP} = 1$ ) frames, the plot in Figure 4.11 shows the dependence of the noise on the number

of Fowler Pairs  $N_{FP}$  used to estimate the signal. By comparing with the dashed line, one can see that the noise does not follow the  $1/\sqrt{N_{FP}}$  dependence expected from uncorrelated “white” noise. Dorn et al. observed a similar behavior [49]. In this case, the reason that the noise does not drop off like  $1/\sqrt{N_{FP}}$  is that the “pink” noise ( $1/f$ ) maintains a non-zero amplitude even after reference pixel subtraction and averaging the multiple samples.

The noise measurements in Figure 4.11 represent the best noise performance obtained with H2RG-001. A limited amount of long, 100 read dark exposures were collected at temperatures between 100-140 K and a substrate voltage of 20 volts. For these data, the CDS noise is slightly larger (10-14  $e^-$ ), but the noise with 30 Fowler pairs reduces to about 2.5  $e^-$ . In certain cases, the read noise bottoms out at this value, with further samples giving no further reduction. In others, the noise actually increases with more samples, most likely because of the  $1/f$  contribution. Again, it should be emphasized that the noise is expected to decrease with decreasing temperature if  $V_{BIASGATE}$  is lowered accordingly.

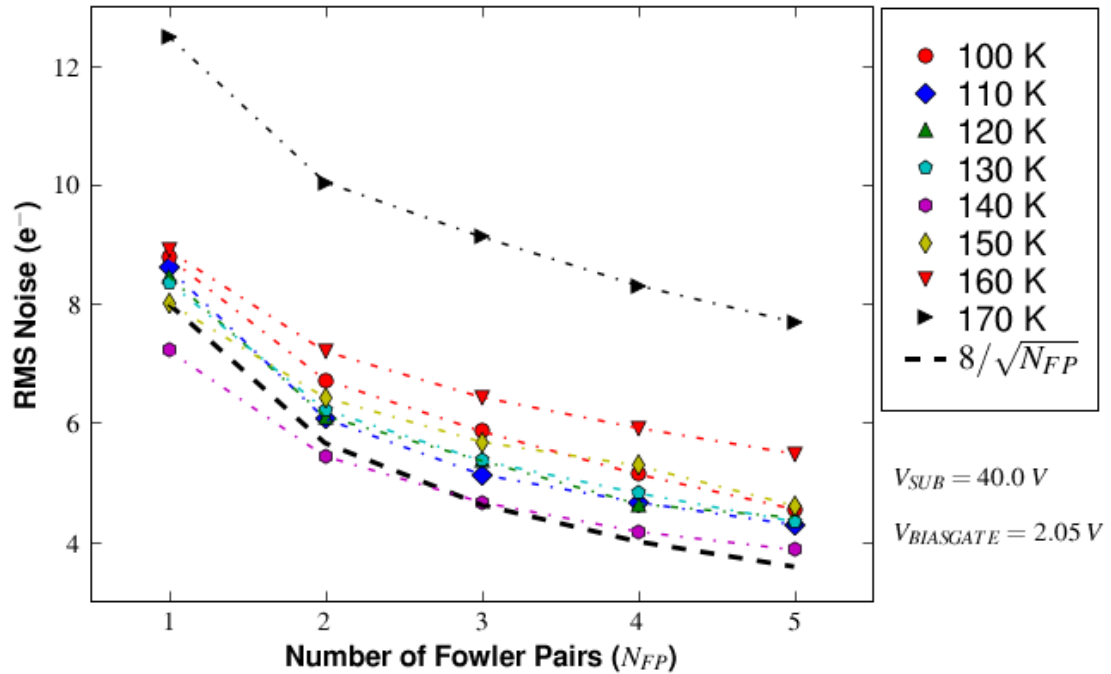


Figure 4.11: Read noise vs. number of Fowler Pairs for a 300x300 window with  $t_{frame} = 1.6$  s on H2RG-001 at temperatures from 100-170 K. The substrate voltage  $V_{SUB} = 40$  V was the highest tested and  $V_{BIASGATE}$  was again held constant at 2.05 V. The noise does not fall off as  $1/\sqrt{N_{FP}}$  (the black dashed line shows  $8 e^-/\sqrt{N_{FP}}$  for comparison) because of the presence of a  $1/f$  contribution.

## 4.5 Dark Current

Dark current is perhaps the greatest bane of astronomical detectors. It decreases the dynamic range of the detector, increases the read noise, and limits exposure times. For practical purposes, any photocurrent signal that produces less charge per unit time than the charge imparted by dark current will be undetectable. In an ideal detector, dark current would not exist, or more accurately, would not make any contribution to the measured signal. Unfortunately, in all known detectors it is coupled with the signal one is trying to measure.

After a hybrid detector has been fabricated, the only “knobs” one has to control the dark current are temperature and bias voltages. Increasing the reset voltage will decrease the dark current in some cases, but doing so will also limit the dynamic range of the pixels. Cooling the detector will drastically reduce the dark current, however, this comes with the cost of decreased quantum efficiency. For this reason, every attempt is made in the design and fabrication of the detector to make the dark current as low as possible.

### 4.5.1 Sources of Dark Current

Dark current is the sum of any thermal leakage currents that will cause the detector to integrate charge even in the absence of light. These leakage currents can arise anywhere in the detector and even the readout circuitry may potentially make contributions to it (the ROIC in the HyViSI exhibits dark current when no detector has been bump bonded to it). The most prominent sources, however, are the detector bulk and the surfaces at the various interfaces.

Since a thorough treatment of dark current in semiconductor imaging arrays is beyond the scope of this thesis, several good references are worth noting. Janesick [3] provides an excellent treatise on dark current in CCDs, much of which is relevant for silicon hybrids. McCaughrean [41] presents a similarly well formed description of dark current in infrared hybrid detectors.

### 4.5.2 Estimating Dark Current

To find an estimate of the dark current over the whole detector at a particular temperature we first adjust the temperature inside the dewar and let it settle to equilibrium. Once settled, we block all light to the detector and take a series of multi-read exposures. The number of reads taken is varied to give results for a range of different exposure times (the cadence is also varied in some cases).

For a set of exposures which all consist of the same number of reads, we take the median value of each pixel over all the exposures in order to reject cosmic ray events and eliminate any spurious electrical signals that may occur. A slope is then fitted to each pixel, yielding an estimate of the number of electrons collected in the pixel due to thermally generated carriers vs. time.

A typical histogram for the final set of dark slopes for H1RG-022 is shown in Figure 4.12. The median, mean, and mode of the distribution all provide a different way of evaluating the dark current.

The **mean dark current** takes into account all of the outliers such as hot, open, and dead pixels. It therefore tends to be the highest of the three estimates. The **median dark current** rejects outliers, but still includes the contributions from regions of the detector that have a higher dark current than the majority of pixels. For instance, the pixels near the edge of H1RG-022 show a slightly higher dark current than the ones near its middle. The **mode of the dark current** gives an estimate for the most commonly occurring dark current, i.e. the peak of the distribution. One must be careful to specify which estimate is being used when comparing dark current values for a given detector. This is especially true in astronomy, where fractions of an electron per second per pixel are significant.

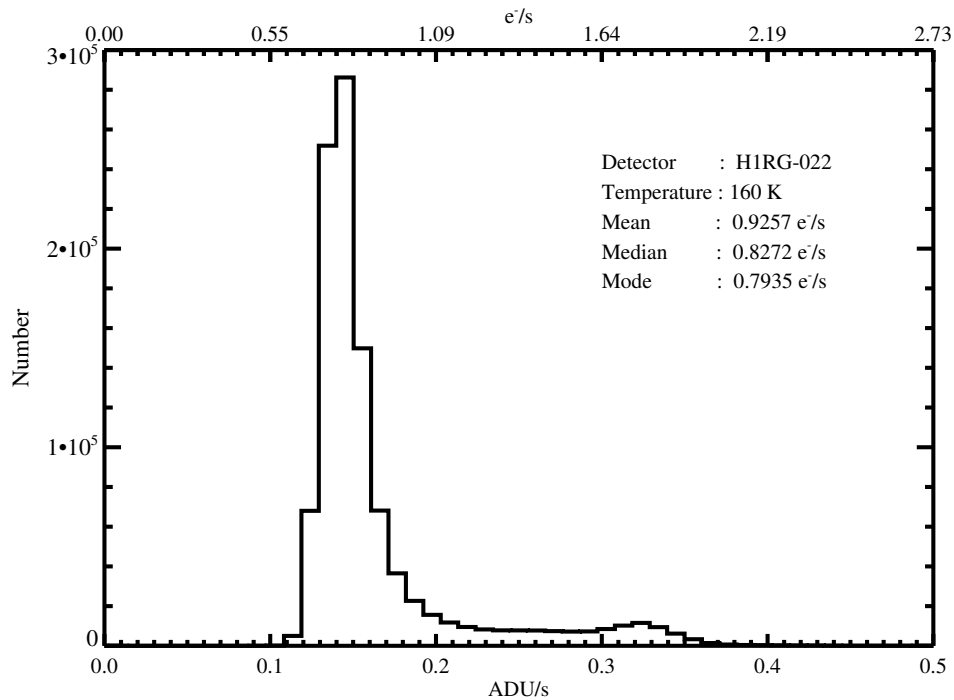


Figure 4.12: A representative dark current histogram generated from a dark exposure slope-fit for H1RG-022. The secondary peak around 0.32 e<sup>-</sup>/s is due to slightly higher dark current around the periphery of the detector.

#### 4.5.2.1 Units of Measurement

One often sees dark current expressed as the number of electrons generated per pixel per second. Because pixels can take any shape or size, a different unit must be used in order to compare different detectors: one that does not depend on the area or geometry of the pixel. For this reason, dark current is usually expressed in terms of electrical current per unit area: a *current density*.

In order to make the conversion between these two commonly used units, we can use the following equation for the dark current,  $DC$ :

$$DC(q/s/cm^2) = \frac{q}{A} * DC(e^-/s/pix), \quad (4.12)$$

where  $q = 1.602 \times 10^{-19}$  Coulombs/ $e^-$  and  $A$  is the area of the pixel expressed in  $cm^2$ . For the  $18 \mu m$  pixels of the H2RG and H1RG detectors, the factor on the right hand side turns out to be about  $q/A = 5 \times 10^{-14}$  (C·pix/ $e^- \cdot cm^2$ ). Thus, a dark current of  $1 e^-/s/pix$  corresponds to roughly  $50 \text{ fA}/cm^2$ .

### 4.5.3 HyViSI Dark Currents

Dark current has been measured for several different HyViSI detectors. Figure 4.13 shows the dark current density measured for H1RG-018, H1RG-022, H2RG-32-147, and H4RG-10-007.<sup>3</sup> While the values below 160K are acceptable for many astronomical applications, the dark current is still rel-

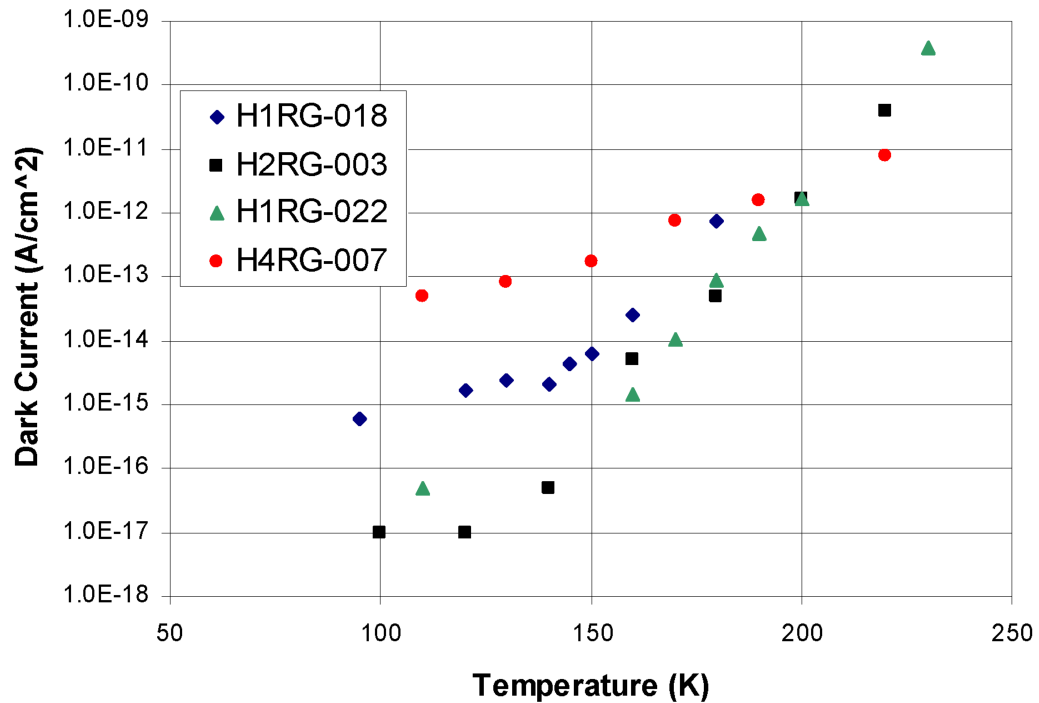


Figure 4.13: Dark current versus temperature for several HyViSI devices. H4RG-10-007 has  $10 \mu m$  square pixels. All other devices have  $18 \mu m$  square pixels.

<sup>3</sup>Results for H1RG-018 were obtained by Don Figer at the Independent Detector Testing Laboratory (IDTL).

atively high. For instance, the HyViSI detectors have to be cooled to 200K to achieve  $1\text{pA}/\text{cm}^2$ , whereas this level of dark current is attainable at  $60^\circ\text{C}$  in CCDs [77]. The exact source of this dark current is not fully understood. Further tests, such as using identical detectors with different thicknesses, testing bare multiplexers without detector layers bonded to them at cryogenic temperatures, and comparing the results for devices with different treatments of the Si-SiO<sub>2</sub> frontside passivation (the processing techniques for each unique device are proprietary to TIS), should help pinpoint where it is generated.

#### 4.5.4 Reset Anomaly in HyViSI

The term *reset anomaly* is used to describe an oddity that has been observed in most, if not all, infrared hybrid detectors. The effect shows itself as a large non-linearity in signal immediately following reset. The non-linearity can be fit with an exponential function that has a time constant ranging from seconds to hours, and although not fully understood, is usually attributed to RC charging effects somewhere in the detector or multiplexer [59].

HyViSI detectors show similar “anomalous” nonlinearities under certain operating conditions. One large nonlinearity is tied purely to a low-voltage pixel reset. We refer to this as the HyViSI reset anomaly. Another is tied to clocking inactivity in the array. If the clocks are stopped during an up-the-ramp integration or while the detector is idle, the pixels exhibit a drop in signal followed by a nonlinear return to the value before the clocking ceased. These two effects show similarities and can be easily mistaken for one another. As shown in the following sections, though, the nonlinearity induced by a low value of  $V_{RESET}$  and that caused by not clocking are two different phenomena. It should also be mentioned that additional nonlinearities arise from persistence and after forward biasing the photodiodes. These topics will be covered in a later chapter.

##### 4.5.4.1 Nonlinearity After Reset

HyViSI detectors show a large nonlinearity in the early reads after the pixels are reset to a voltage  $V_{RESET}$  below about 150mV. The ramp for each pixel, an example of which is shown in Figure 4.14, can be fit with a 4 parameter function of the form:

$$S(i, j, t) = S_o(i, j) + A_{i,j}(1 - \exp^{-t/\tau_{i,j}}) + B_{i,j}t \quad (4.13)$$

The parameters  $A$ ,  $B$ ,  $S_o$ , and  $\tau$  vary greatly over the array. This is partly because the fit is not very good for most pixels; it shows a large  $\chi^2$  value for the majority of pixels.  $B_{i,j}$  should represent the dark current in equilibrium, but in most cases it overestimates the dark current by an order of magnitude. Nevertheless, the values  $A$  and  $\tau$  are useful indicators of the voltage swing (or the equivalent change in pixel carrier density) and how long the effect takes to subside.

The low  $V_{RESET}$  reset anomaly only occurs in the science pixels. The reference pixels are not

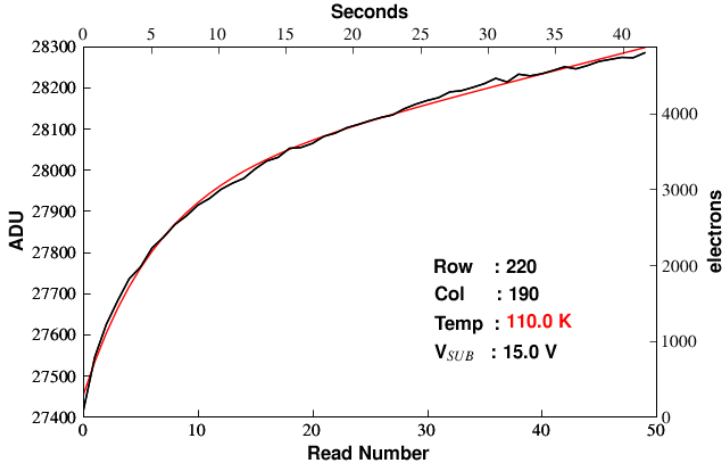


Figure 4.14: The black curve shows the signal of pixel (190, 220) in an up the ramp dark exposure. The non-linearity occurs for values of  $V_{RESET} < 150mV$ . The red curve is the fit from Equation 4.13 with  $A = 442$ ,  $B = 6.0$ ,  $\tau = 5.3$ , and  $S_o = 27453$ .

affected. Further, it shows a definite spatial correlation with the ROIC outputs, as can be seen in Figure 4.15. This suggests the effect occurs in the detector bulk or the interface between the detector and multiplexer. One possibility is that the setting  $V_{RESET}$  sufficiently low causes the n type surface above the  $SiO_2$  layer to invert and collect holes during the actual reset. When the reset is finished and the pixels begin to integrate, these holes then diffuse back to the  $p^+$  implants and cause the rise in signal. The spatial pattern would then be explained by variations in the surface potential as a function of distance away from the output buses.

#### 4.5.4.2 Nonlinearity After Inactivity or Change in Mode of Operation

The HyViSI pixels show another unexpected, nonlinear behavior after periods of inactivity, after resets under certain operating conditions, or during a fast sequence of resets and reads of the detector. In any of these cases, the reference pixels and the science pixels exhibit the effect, indicating that it arises in the ROIC. It is therefore likely an electrical effect and not due to leakage currents, but it is included here because it is an effect that can easily be mistaken for elevated dark current.

By inactivity, we mean that the pixels are not being clocked. This may occur unintentionally between exposures because of a bug in assembly code or it may occur intentionally as part of an observing strategy. An example of the latter would be a pause in clocking during the wait period of a Fowler Sampling ramp designed to save power. The problem is that if the clocking of the pixels cease after some time  $t_1$  and then start again at  $t_2$  during a ramp, the pixel values will show a large drop between the two times. The drop ranges from 5-10 mV in the cases we have observed.

We also see the effect when we operate the detector in window mode and take a series of exposures without doing idle resets between the exposures. And it shows up strongly when the value of  $V_{BIASGATE}$  is changed between exposures. The effect has a strong temperature dependence, which might be attributed to the dependence of the drain current in the unit cell source follower.

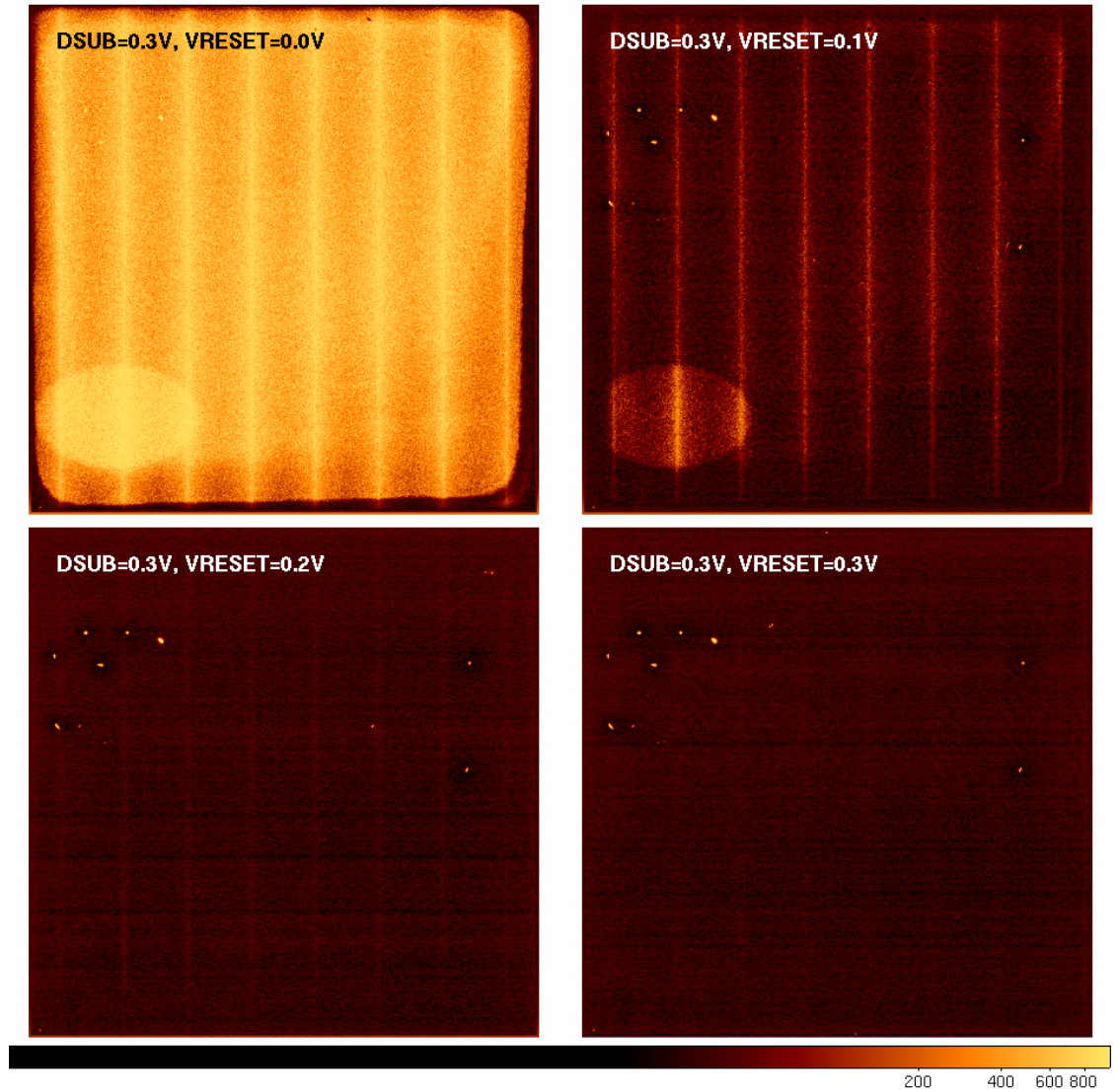


Figure 4.15: Images formed by subtracting the first read from the last read of 50 read ramps taken by H1RG-022 at 100K. A log scale is used for the stretch. The images clearly show that for values of  $V_{RESET}$  below 150 mV, the dark current signal is very large. They also show that a spatial pattern that suggests that pixel voltages are coupled to the output column buses.

## 4.6 Quantum Efficiency

There are several different definitions of Quantum Efficiency (QE) available in the literature. But for most intents and purposes, the QE of a detector can simply be thought of as the fraction of incoming photons that are converted to electron-hole pairs and collected as signal. When characterizing a detector, one measures the QE as a function of wavelength in a certain wavelength range, and this serves as a good indicator of how sensitive the detector is to these wavelengths.

### 4.6.1 PIN Diode Quantum Efficiency

The QE in the PIN diode detector layer of the HyViSI is determined by a number of different factors. Before the photons have a chance to be absorbed in the detector bulk, they must make it past the back surface of the detector. An anti-reflection coating is applied to this surface to minimize the fraction of photons that are reflected,  $R$ . Photons with wavelength  $\lambda$  that make it inside the detector then travel for some characteristic *absorption length*,  $\alpha(\lambda)$ , before they are converted into an electron-hole pair.<sup>4</sup> If we assume that the detector is fully depleted so that  $W_D$  is equal to the detector thickness, and that all photons absorbed in the depletion region are collected as signal, then we can express the QE as:

$$QE = (1 - R) [1 - \exp(-\alpha W_D)] \quad (4.14)$$

This equation, which is similar to the one in Sze [53] except that the diffusion of the minority carriers has been neglected, reveals the benefit of the thick  $W_D = 100 \mu\text{m}$  silicon in the HyViSI.

### 4.6.2 HyViSI Detective Quantum Efficiency (DQE)

DQE is the realized S/N compared to that of an ideal detector. It is often measured in the background-limited case so that it is most closely related to the photon capture process in the bulk material of the detector, as opposed to being related to read noise effects in the post-capture electronics. DQE can vary with wavelength, temperature, and individual pixel properties. To measure it, we illuminate the detector with a monochromatic flat field produced by an integrating sphere and monochromator. The light is monitored by a calibrated silicon photodiode located at a port on the integrating sphere. A similar calibrated diode is placed at the location of the detector in order to transfer the flux measured at the integrating sphere to the focal plane. Once this wavelength-dependent calibration is made, the detector is then placed at the focal plane and the experiment is repeated.

The results of our measurements for H4RG-10-007 and others obtained for H2RG-003 are shown in Figure 4.16. For QE measurements of an H2RG HyViSI below 800 nm, the reader is referred to

<sup>4</sup> $\alpha(\lambda)$  is defined as the depth in the material at which 1-1/e of the incident photons of wavelength  $\lambda$  have been absorbed.

Dorn et al. [78]. As can be seen in Figure 4.17, because the QE measurement involves illuminating the detector with a narrow wavelength range, interference fringes are observed in the illumination pattern. The fringes are strongest near  $1 \mu\text{m}$  and show up similarly when a  $y$  band filter is used on broadband light. Removing them with “generic” flat fields is not trivial because the pattern depends on the angles of the incident rays. The best results are obtained when the flats are taken with a very similar illumination source to the one present during the science exposures (see Section 5.2.5).

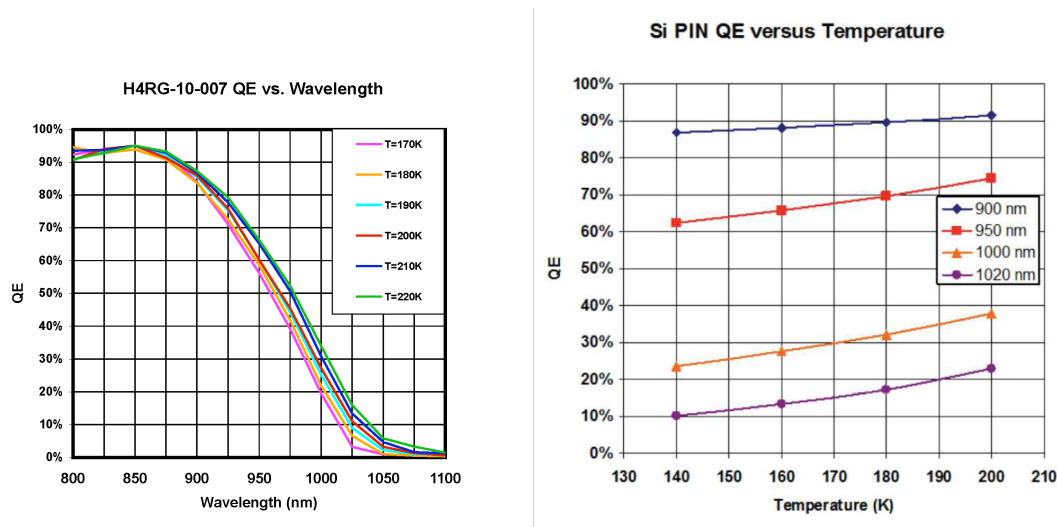


Figure 4.16: H4RG-10-007 relative QE versus wavelength (left) and H2RG-003 relative QE versus temperature (right) near the long wavelength cutoff. The results show that QE increases with temperature and are consistent with a silicon detector having  $100 \mu\text{m}$  thickness.

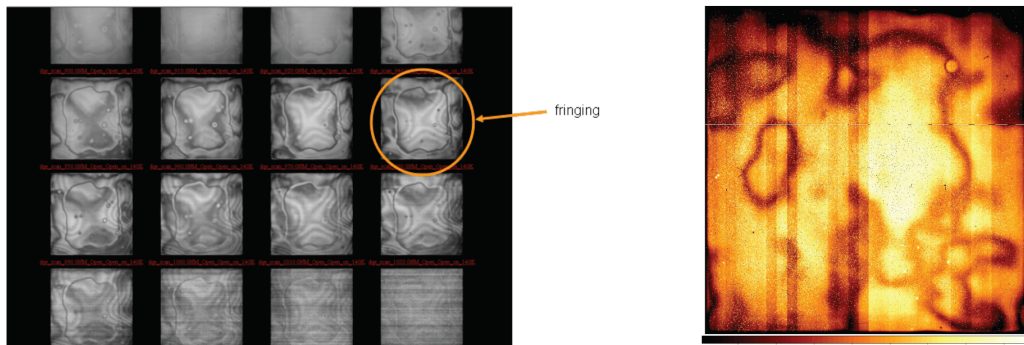


Figure 4.17: Fringing seen in monochromatic flat field images near  $1 \mu\text{m}$  obtained with the H2RG-003 device (left). The fringing indicates thickness variation of a few microns. Fringing for the H4RG-10-007 device (right). The columnar striping is an artifact of electronic readout offsets and is not a QE variation of the detector.

## 4.7 Linearity/Well Depth

Linearity is one of the most important detector properties for astronomical purposes. Accurate photometry can only be performed if a detector has a stable, well-known response to varying brightnesses and integration times. While the term *linearity* implies the response should have a linear relationship to both of these quantities, this is often not the case. Infrared detectors, for instance, show a decreasing response in signal as they get closer to saturation: the nodal sensitivity actually decreases as the capacitance grows larger.

While it is generally possible to correct for nonlinear behavior by properly characterizing the pixel response, this adds one more step to the already elaborate data reduction process employed in astronomy. One would prefer to start with a detector that has an intrinsically linear response to light. And for this reason, linearity is usually listed as a standard detector specification along with the read noise, quantum efficiency, and dark current.

Linearity, or an equivalent nonlinearity, is defined in several different ways throughout the literature [41, 3, 79]. In the end, all of the definitions convey the deviation of an overall conversion gain  $G_{NET}$  ( $e^-/ADU$  or  $e^-/DN$ ) from some average value. The deviation might arise as the signal integrates for a given brightness or it may occur at a given signal level when the brightness is varied. Usually what is quoted is the ratio of the deviation in  $G_{NET}$  to its average value, expressed as a percentage. A detailed linearity curve will show this deviation as a function of signal level, and for a number of flux levels.

Any one of the factors in Equation 4.3 can contribute to nonlinear behavior. Janesick divides nonlinearity into two distinct categories:  $V/V$  nonlinearity and  $V/e^-$  nonlinearity [79], based upon which of these gain factors is contributing. If the capacitance of the pixel  $G_{PIXEL}$  is changing, the nonlinearity is said to be  $V/e^-$ . If any of the other four gains,  $G_{UC}$ ,  $G_{OUT}$ ,  $G_{AMP}$ , or  $G_{A/D}$  is changing, then the nonlinearity is said to be  $V/V$ . Usually  $V/V$  nonlinearity is attributed to the pixel source follower amplifier ( $G_{UC}$ ), but for HxRG multiplexers, the output source follower ( $G_{OUT}$ ) is also a suspect as it relies on an external current source.

For any detector that integrates photocharge on a pixel capacitance, the signal response will eventually become nonlinear as the pixel “well” nears its maximum capacity. The maximum capacity of the pixel, in units of electrons, is referred to as the *well depth*. Photoelectrons or holes generated above a pixel that has reached its well depth will either bloom into neighboring pixels or, for certain architectures, be dissipated by an anti-blooming diode or drained by the pixel reset FET (if it is held in a soft reset mode).

### 4.7.1 Sources of Nonlinearity in HyViSI Detectors

It was shown in Section 2.2 that the fractional change in nodal capacitance for the HyViSI due to the change in spacing between the diode “capacitor plates” is negligible when compared to the other

capacitances. For this reason,  $V/e^-$  nonlinearity is not expected to be a primary contributor in the HyViSI pixels. This expectation is confirmed in photon transfer curves obtained with H2RG-32-147 and H1RG-022, examples of which are shown in Figure 4.18. If  $V/e^-$  nonlinearity was present, the fixed pattern noise should deviate from a slope of 1 (in a log-log plot). This is not observed. Instead, the shot noise deviates from a slope of  $1/2$ , which indicates that  $V/V$  nonlinearity is the culprit.

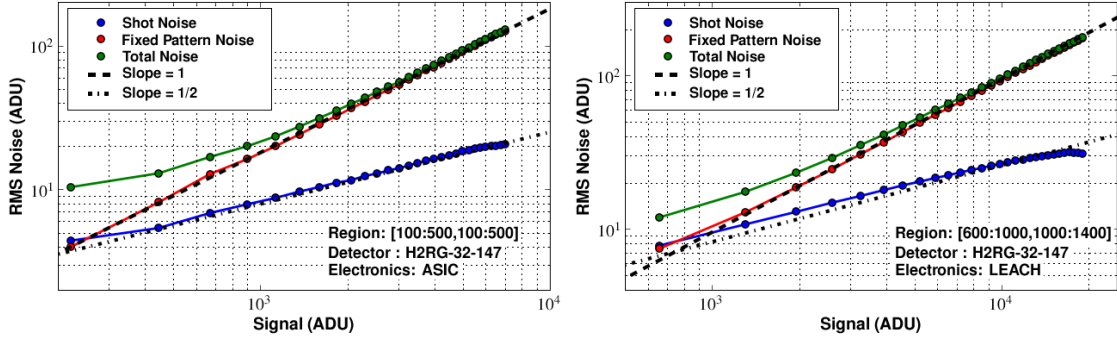


Figure 4.18: Photon Transfer Curves for H2RG-32-147 using the SIDECAR ASIC (left) and ARC (right) electronics. The curves were generated from flat field images obtained at the Kitt Peak 2.1m telescope. The total noise is shown by the green curve. After subtracting read noise in quadrature, total noise curve is broken down into shot noise (blue) and fixed pattern noise (red), following Janesick [79]. Also shown are lines with slope  $1/2$  and  $1$ , which should correspond to shot and fixed pattern noise, respectively. The deviation in shot noise from slope  $1/2$  indicates  $V/V$  nonlinearity.

The two primary suspects for the  $V/V$  nonlinearity are the pixel source follower, through a changing  $G_{UC}$ , and the output source follower, through a changing  $G_{OUT}$ . Measurements made with a known voltage source input to the SIDECAR and ARC electronics show that the gains  $G_{AMP}$  and  $G_{A/D}$  vary by less than  $0.5\%$  over the full voltage range of the  $A/D$  converter, so these terms can be safely ignored. The control electronics may still contribute to nonlinearity in cases where the output buffer SF is used, though, since they provide it a current source. And if an external voltage on the control electronics (as opposed to one coming from the multiplexer) is used as a reference for the pixel voltages, any oscillations, sagging, etc. on the reference voltage will result in nonlinear behavior. These sources will be elaborated upon further in the next section.

#### 4.7.2 Measurements of Nonlinearity in HyViSI Detectors

Numerous linearity measurements have been reported for HyViSI detectors. Dorn et al. report a  $5\%$  nonlinearity for an H2RG HyViSI over a  $90,000 e^-$  well [49] and Figer et al. report a  $1\text{-}2\%$  linearity for a similar H2RG device [80]. Simms et al. report a very high nonlinearity for an H4RG HyViSI of about  $10\%$  over its full  $55,000 e^-$  well. The large disparity among the numbers suggests that the

nonlinear behavior is not an intrinsic property of the imager, but instead depends on the operating conditions such as bias voltages and currents.

Unfortunately, a thorough study has not been performed to determine the configuration that minimizes nonlinearity in HyViSI imagers. From first principles, though, several bias voltages and additional sources should be relevant:

- 1) **The biasing to the pixel source follower FET** is especially critical to the linearity of the output and may be the primary source of the discrepancy between the reported values. Because the drain current changes over the signal range, the transconductance  $g_m$  will also vary. This, in turn, will induce a change in the output impedance [81], resulting in nonlinearity. Since the output impedance goes like  $1/g_m$ , the situation is improved for higher transconductance. And for the case of the HyViSI, this means that a lower  $V_{BIASGATE}$  should result in better linearity because of a higher drain current and higher transconductance.
- 2) **The biasing to the output source follower FETs** is also very critical if they are included in the signal path. When operated in buffered mode, the HxRG detectors require an external current source or pull-up resistor as a load for the output FETs, and the more this load deviates from an ideal current source, the more the response will deviate from a linear one.
- 3) **Charge injection for low  $V_{RESET}$**  will cause the pixels to have an exponential ramp until their voltage reaches about 150 mV. Unlike the previous two sources, this one can be removed with a dark current subtraction.
- 4) **A changing reference voltage on the control electronics** will cause nonlinearity if it is used for differential measurements of the analog outputs. For instance, if  $V_{REFMAIN}$  on the SIDECAR ASIC oscillates independently from the bias voltages to the multiplexer, the measured pixel voltages will appear to oscillate. This source can be eliminated by using the reference output  $V_{REFOUT}$ .
- 5) **Output coupling** may result in nonlinearity for all of the pixels selected at a given time. The large signal from an over-saturated pixel in one channel will cause an increase in the signals from all of the pixels in the other outputs.
- 5) **Coupling of the pixel node voltage to the supply voltage, reset FET gate, etc.** will cause the measured pixel voltages to deviate from the “true” voltage that would be generated purely by the charge stored on the nodal capacitance. Moore found significant coupling of the nodal capacitance to the unit cell supply, row enable gate, and reset gate [24]. While similar measurements were not carried out on the HxRG multiplexers as part of this dissertation, it is physically reasonable to assume that similar couplings exist. The reference pixels on the HxRG devices provide a means to subtract some of these couplings.

Linearity measurements for H4RG-10-007, H1RG-022, and H2RG-32-147 were made using flat field UTR exposures in which both the brightness of the source and the integration time were varied. All of these exposures were taken with the output buffer FETs in the signal path since the electronics were separated from the HxRGs by about 18" of cable. The ARC electronics uses a pull-up resistor and the SIDECAR ASIC uses a current source in the preamp circuitry to provide the drain current for the output FETs. The current provided by both should be between 300-600  $\mu\text{A}$ . Measurements on H2RG-001 were made without the output FET in the signal path since a cold SIDECAR was located very close to the detector. However, the LED used to illuminate the detector resulted in very nonuniform illumination, and as a result only very small regions could be used to measure similar signal levels.

To measure the linearity from a given exposure, the mean signal for a small region of pixels was calculated for each nondestructive read (after bias subtraction), yielding an average signal  $\overline{S}_r$  as a function of exposure time  $t_r$ . To generate the plots shown in Figure 4.19, the slopes  $\overline{S}_r/t_r$  are normalized to  $\overline{S}_1/t_1$  and plotted at  $S_r$ .

Following the discrepancy in measurements made by different authors, the plots in Figure 4.19 show dramatic differences, even for the same detector. This further supports the theory that non-linearity in HyViSI devices is due mainly to points 1-6 listed above rather than a changing nodal capacitance. The linearity measured for H2RG-32-147 with the SIDECAR ASIC is particularly poor compared to that measured with the ARC electronics. While  $V_{BIASGATE} = 2.29$  V is significantly higher for the former, Figer et al. measured 1-2% nonlinearity with  $V_{BIASGATE} = 2.4$  V, suggesting that this voltage is not responsible for the difference. A similar argument can be made for  $V_{BIASPW}$ . The remaining possible sources are the current to the output source follower and reference voltage used to measure the analog video outputs of the detector. If  $V_{REFMAIN}$  on the SIDECAR was the source of the nonlinearity, subtracting the reference pixel voltages should reduce the nonlinearity uniformly across the signal range. Since this is not the case, it can be concluded that the current source to the output source follower is primarily responsible for the difference between the second and third plots.

The output buffer FET is eliminated from the measurement for H2RG-001 shown in the first plot. Although the signal range of the detector is limited to half of the full well—using a higher gain and  $V_{REFOUT}$  resulted in the signal clipping the upper rail of the ADC—the linearity is good to  $< 1\%$  after reference pixel correction in this case. Extrapolating the curve suggests that it will remain within 1% over the full well, which further bolsters the argument that the output source follower or the current source it uses is primarily responsible for the nonlinearity in the HyViSI detectors. Further experiments should be undertaken to verify this.

The plots in Figure 4.19 do not indicate exactly what flux level was used to illuminate the detectors. However, measurements made between 500 – 10,000  $e^-/s$  all yield similar results. Measurements for very low flux levels need to be performed to verify linearity at very small signal levels.

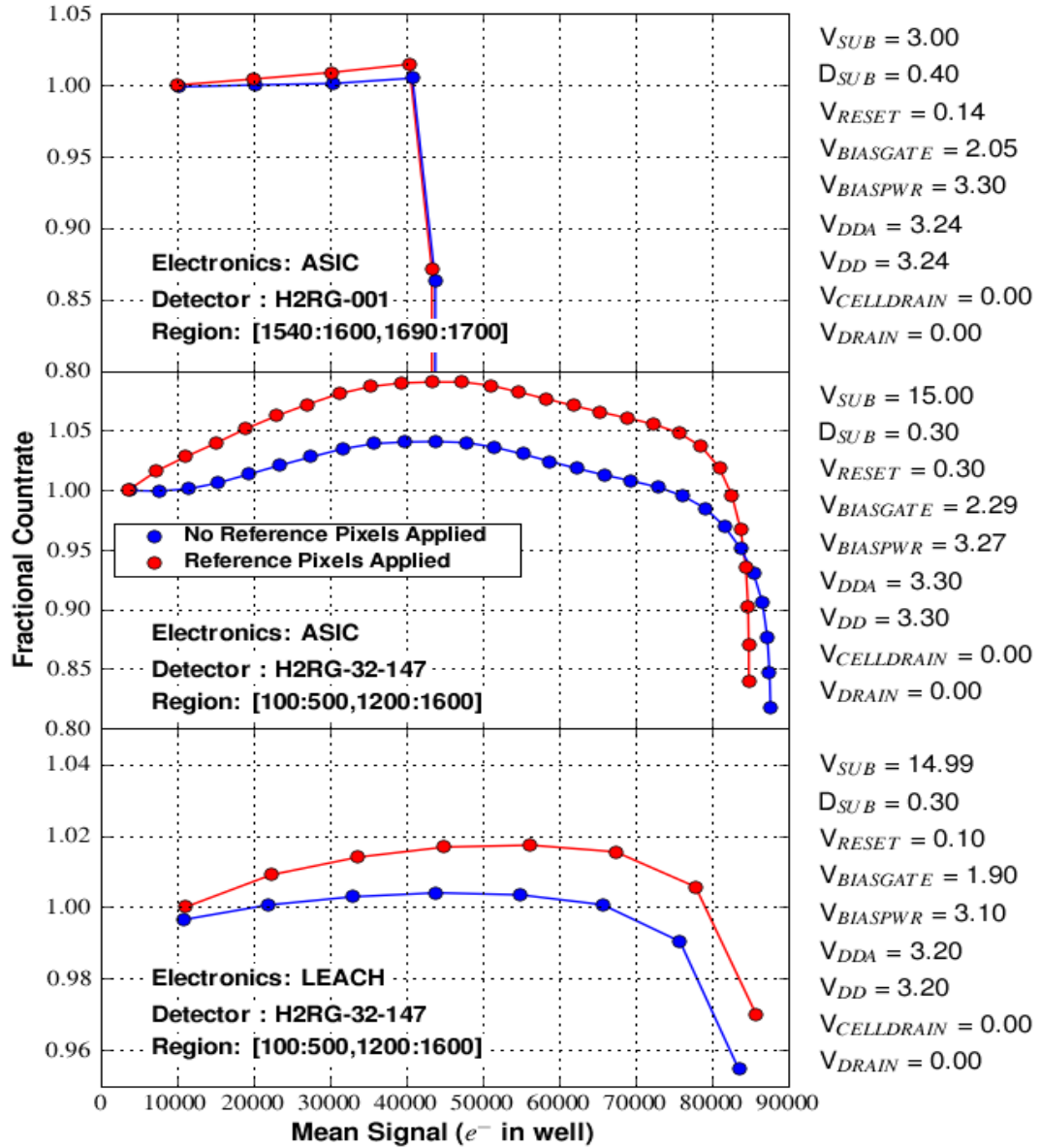


Figure 4.19: Linearity of H2RG-001 and H2RG-32-147 as a function of signal accumulated in pixel. H2RG-32-147 measurements were made with the output source follower in the signal path; those for H2RG-001 were made without it. The region for H2RG-001 was very small because the illumination was quite nonuniform over the detector and the linearity cuts off at 45,000  $e^-$  because the pixel voltages were out of range for the SIDECAR ADC. The bias voltages used for the measurements are listed to the side of each plot in units of volts. The output source follower and  $V_{BIASGATE}$  appear to have the largest effect on the linearity.

### 4.7.3 HyViSI Well Depths

A large pixel well depth is highly desirable in astronomy as it allows for large dynamic range imaging. If the wells are small, bright stars may fill them before the pixels are read, preventing an estimate of their luminosity. In theory, the well depth,  $WD$ , should be determined by the doping of the active collecting volume for the photogenerated charge. For the case where holes are collected:

$$WD = V * N_A, \quad (4.15)$$

where  $V$  is the volume of the collecting region and  $N_A$  is the acceptor density. However, this prediction is rarely, if ever, met in CCD or CMOS detectors [3]. The HyViSI pixels are no exception. If the  $p^+$  implant in the pixel has a depth of  $1 \mu\text{m}$ , a size of  $9\text{-}18 \mu\text{m}$  on a side, and an acceptor concentration of  $N_A = 10^{14} - 10^{19} / \text{cm}^3$ , the well depth is expected to be  $WD = 10^7 - 10^{10} e^-$ . This is far in excess of the typical measured values on the order of  $10^5 e^-$ .

In addition to the pixel structure, the well depth should depend on the reset voltage  $V_{RESET}$ . The maximum depth is achieved when  $V_{RESET} = 0 \text{ V}$  is at its minimum value and the reverse bias of the PIN diode is at its maximum. However, the exponential dark current mentioned in Section 4.5.4.1 makes values of  $V_{RESET} < 150 \text{ mV}$  impractical.

The well depth can be measured from the same exposures used to generate the linearity curves in the previous section. Piecewise slopes  $(S_{r+1} - S_r)/(t_{r+1} - t_r)$  are calculated between consecutive reads and normalized to the one calculated from a slope fit (see Section 5.2.4). The pixels are deemed saturated at a signal where their normalized slopes fall below 0.9. The mean of the saturation signal level is then taken to be the average well depth. Results for the HyViSI sensors H1RG-022, H2RG-32-147, and H4RG-10-007 are listed in Table 4.5. The low well depth for H1RG-022 relative to that of H2RG-32-147 is not understood since the pixel layout should be similar in the two devices.

Table 4.5: Well Depths for several HyViSI detectors along with pixel size and the value of  $V_{RESET}$  at which they were measured. The pixel responsivity,  $G_{PIXEL}^{-1}$ , is discussed in Section 4.3.

	H1RG-022	H2RG-32-147	H4RG-10-007
Pixel Size ( $\mu\text{m}$ )	18	18	10
$V_{RESET}$ (mV)	90	100	100
Well Depth ( $e^-$ )	55,000	85,000	55,000
$G_{PIXEL}^{-1}$ ( $\mu\text{V}/e^-$ )	10.53	10.61	25.21